ARMY RESEARCH LABORATORY

Experimental Studies of the No. 41 Primer and Ignition of 5.56-mm Ammunition

by Anthony W. Williams, Andrew L. Brant, Pamela J. Kaste, and Joseph W. Colburn

NOTICES

Disclaimers

Army Research Laboratory

Aberdeen Proving Ground, MD 21005-5066

Experimental Studies of the No. 41 Primer and Ignition of 5.56-mm Ammunition

**Anthony W. Williams, Andrew L. Brant, Pamela J. Kaste,
and Joseph W. Colburn**
Weapons and Materials Research Directorate, ARL

REPORT DOCUMENTATION PAGE

Form Approved
OMB No. 0704-0188

Public reporting burden for this collection of information is estimated to average 1 hour per response, including the time for reviewing instructions, searching existing data sources, gathering and maintaining the data needed, and completing and reviewing the collection information. Send comments regarding this burden estimate or any other aspect of this collection of information, including suggestions for reducing the burden, to Department of Defense, Washington Headquarters Services, Directorate for Information Operations and Reports (0704-0188), 1215 Jefferson Davis Highway, Suite 1204, Arlington, VA 22202-4302. Respondents should be aware that notwithstanding any other provision of law, no person shall be subject to any penalty for failing to comply with a collection of information if it does not display a currently valid OMB control number.
PLEASE DO NOT RETURN YOUR FORM TO THE ABOVE ADDRESS.

1. REPORT DATE *(DD-MM-YYYY)*	2. REPORT TYPE	3. DATES COVERED (From - To)
September 2006	Final	January 2005–February 2006

4. TITLE AND SUBTITLE	5a. CONTRACT NUMBER
Experimental Studies of the No. 41 Primer and Ignition of 5.56-mm Ammunition	
	5b. GRANT NUMBER
	5c. PROGRAM ELEMENT NUMBER
6. AUTHOR(S)	5d. PROJECT NUMBER
Anthony W. Williams, Andrew L. Brant, Pamela J. Kaste, and Joseph W. Colburn	662618.H8099
	5e. TASK NUMBER
	5f. WORK UNIT NUMBER

7. PERFORMING ORGANIZATION NAME(S) AND ADDRESS(ES)	8. PERFORMING ORGANIZATION REPORT NUMBER
U.S. Army Research Laboratory ATTN: AMSRD-ARL-WM-BD Aberdeen Proving Ground, MD 21005-5066	ARL-TR-3922

9. SPONSORING/MONITORING AGENCY NAME(S) AND ADDRESS(ES)	10. SPONSOR/MONITOR'S ACRONYM(S)
Project Manager-Maneuver Ammunition Systems Picatinny Arsenal, NJ 07806-5000	
	11. SPONSOR/MONITOR'S REPORT NUMBER(S)

12. DISTRIBUTION/AVAILABILITY STATEMENT

Approved for public release; distribution is unlimited.

13. SUPPLEMENTARY NOTES

14. ABSTRACT

Understanding the underlying physics of the ballistic event is important to gun system design and in determining corrective measures necessary to address unexpected results (misfires, variations in muzzle velocity, projectiles stuck in-bore, etc.). The present study characterizes the output of the small-caliber primer (no. 41) in open-air and ballistic simulator experiments and full-scale gun firings. Through the analysis of high-speed digital photography data, pressure-time data and particles recovered from the primer, the small-caliber primer and ignition system have been characterized. The open-air experiments reveal the primer particle size, velocity, and composition. These data are used in a separate and parallel effort to develop a detailed primer model in which both gas and particle features are captured. A series of tests were also conducted using a ballistic simulator fixture. The fixture incorporates an acrylic chamber that simulates the 5.56-mm ammunition geometry. The primer output is characterized by measuring the pressure-time response within the simulator chamber. High-speed videos of flamespreading due to the primer indicate that the flame front penetrates no more than 40% of the propellant bed. In addition, there is evidence that the propellant bed is compressed in the region near the base of the projectile. Gun firings were conducted in which pressures were measured inside the chamber and at the case mouth. In-bore radar data were collected and correlated with the pressure-time response measured in the chamber. From these data, it was determined that the projectile begins to move into the gun tube at a pressure between 20 and 30 MPa. Case mouth pressures and projectile velocities were within the specifications for the M855 small-caliber round. The experimental work discussed herein is being used to validate a detailed small-caliber primer model and an ARL-NGEN CFD model.

15. SUBJECT TERMS

small-caliber, propulsion, ballistic simulator, no. 41 primer, flamespreading

16. SECURITY CLASSIFICATION OF:			17. LIMITATION OF ABSTRACT	18. NUMBER OF PAGES	19a. NAME OF RESPONSIBLE PERSON Anthony W. Williams
a. REPORT	b. ABSTRACT	c. THIS PAGE	UL	46	19b. TELEPHONE NUMBER *(Include area code)*
UNCLASSIFIED	UNCLASSIFIED	UNCLASSIFIED			410-278-6122

Standard Form 298 (Rev. 8/98)
Prescribed by ANSI Std. Z39.18

Contents

List of Figures

List of Tables

Acknowledgments

1. Introduction

A Project Manager-Maneuver Ammunition Systems funded effort is ongoing to characterize the small-caliber no. 41 primer and the details of its role in the 5.56-mm ammunition's interior ballistics cycle. The recent interest in the no. 41 primer stems from the U.S. Army's interest in reducing the 5.56-mm ammunition's impact on the environment associated with practice range clean up.

The present 5.56-mm ammunition design (M855) has proven effective for many years. Both muzzle velocities and pressure-time histories (typically measured at the case mouth) have been measured to characterize the basic ammunition performance (*1*). However, while the ammunition has been demonstrated for many years to be effective, the Army's investigation of potential changes to the round suggests the need for a detailed understanding of the underlying physics of the 5.56-mm ignition system. In the case of the cartridge ignition and interior ballistics, such understanding has repeatedly been demonstrated to be valuable in medium to large-caliber gun systems (*2–4*).

Insight into the ignition behavior of larger gun systems has been gained through analysis of the early ignition phenomena and the performance of the associated primers (*2*, *5*). Additionally, the details of the flame spreading and pressurization along the gun chamber can be indicative of the overall propulsion system performance (*6*).

Detailed experimental data are needed that characterize the percussion ignition of the primer material, combustion behavior of the neat primer material, the interaction of the material venting from the primer with the propellant, the subsequent ignition of the propelling charge, the further consumption of the charge as regulated by the motion of the projectile, and the pressure driven interactions between the projectile, the case to which it is mechanically bonded, and the gun tube surface on which it inelastically deforms.

The present analysis of the no. 41 primer is coupled between both experimental and modeling efforts. It is believed that this approach will provide an understanding of the 5.56-mm ammunition ignition train and provide for quick analysis of variations in the ammunition design (primer, charge and geometry details). The focus of this report is the experimental characterization. However, the experiments are designed to provide insights into and validation of a detailed primer model. CFD codes like the U.S. Army Research Laboratory's NGEN code do not include a detailed model of the primer (*7*). Instead, NGEN relies upon "look-up" tables for the primer input.

The no. 41 primer was experimentally investigated, in part, by Kuo et al. (*8*), at which time three different percussion primers were studied in an effort to characterize and compare their respective output. The Kuo et al. study utilized a small chamber vented by a nozzle to control

the flow of the primer output. It was determined that about 100 μs were required for the no. 41 primer to consume its constituents. Mass flow rates were calculated and rather large pressures were measured. It was also noted that a large percentage of the no. 41 primer products were in the condensed phase. An understanding of this primer and the process by which it ignites a propellant bed will likely include an understanding of its convective, radiative, and conductive contributions.

The study of primers in open-air has been a standard tool in analyzing primer output characteristics independent of the gun environment in which it operates (*2, 9*). The first phase of this study was focused on open-air primer firings in which high-speed video of the primer initiation event was recorded and particles were recovered for analysis. The aim of the particle analysis is to identify the composition of the particles and understand the relative contribution they may have in propellant ignition.

Figure 1 schematically illustrates the primer cup/anvil assembly studied and discussed in the present work. The primer assembly consists of a primer cup which contains the neat primer material (primer material dry weight = 25.3 mg [0.390 gr]). A thin (approximately 0.09-mm [0.0035-in] thick) sealing paper and lacquer are applied before the anvil is fitted into place. Lead styphnate is the primary explosive used in the primer. The primer output is to be characterized in a manner consistent with supporting the development and validation of a model of the propulsion system.
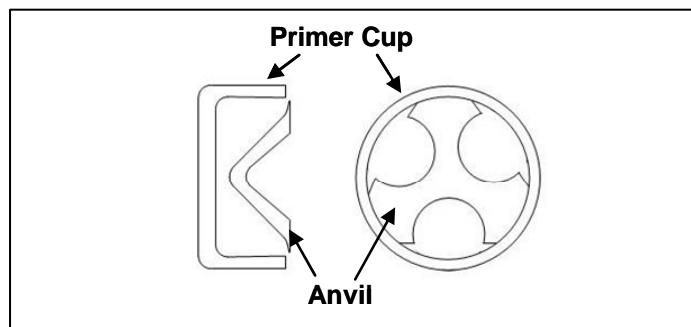
Figure 1. Assembly of 5.56-mm percussion primer.

Additionally, a small-caliber ballistic simulator was utilized to characterize the chamber pressurization and flame spreading due to the primer only. Empty, inert propellant and live propellant experiments are conducted with the ballistic simulator to investigate various phases of the primer-propellant interaction. Both flame spreading and pressurization data from the simulated gun chamber were observed and discussed.

Finally, full-scale instrumented gun firings were conducted. Pressure-time histories, in-bore projectile movement, and velocities were measured. The gun firing data are correlated with relevant details from the simulator data to gain a thorough understanding of the M855 cartridge ignition system.

2. Experimental Setup

2.1 Open-Air Primer Experiments

The experimental data discussed in the present work were obtained using a test fixture which was machined to simulate the 5.56-mm primer cavity geometry. The experimental fixture included a right cylindrical hole (diameter = 2.03 mm [0.080 in]; depth = 1.65 mm [0.065 in]) through which the primer vents into the cartridge/propellant bed in the full cartridge or in the case of the present experiments, the primer vents into open air.

A solenoid was utilized to drive a firing pin which initiated the primer. The primer output was vented through the right-cylindrical hole and into open air or against a witness plate located at fixed distances from the primer (see figure 2a).

For all of the primer experiments, high-speed digital video was recorded of the primer event. A Phantom[*] V5.0 high speed camera, fitted with a 50-mm Nikon-mount lens, was employed to record the visible light produced by the primer. The camera was set to a frame rate of 7400 frames per second (fps) with an exposure of 110 µs to maximize the visible light for a reasonable frame rate. Additional experiments were conducted with settings ranging up to 22,000 fps and with exposures as short as 35 µs to maximize the details recorded of the primer output (additional frames).

A series of experiments was conducted utilizing a witness plate located 64 mm (2-1/2 in) or 121 mm (4-3/4 in) from the primer plate face (distances are labeled "standoff" in figure 2a). The witness plate consisted of an aluminum plate covered with commercial grade aluminum foil. The primer exit hole was recessed 2.5 mm (0.10 in) behind the primer plate face, thus adding 2.5 mm to the distance between the primer and the aluminum witness plate (actual distance between primer vent hole and aluminum plate = 66.5 and 123.5 mm).

Additional experiments were conducted in which double-stick tape was adhered to the aluminum foil witness plate. The tape was in the shape of a disk (diameter = 25.4 mm; thickness = 1/4 mm) and made of carbon. The largest surface of the disk was oriented perpendicular to and in the center of the primer flow axis. For these particular experiments it was expected that particles venting from the primer would adhere to the tape and be available for further analysis. The standoff distances for this series of experiments were 66.5 and 123.5 mm.

Figure 2b illustrates the camera orientation for additional open-air primer experiments which were performed. The camera was located forward of the primer and oriented to view the primer event along the primer flow axis.

---

[*] Phantom is a registered trademark of Vision Research, Inc., Wayne, NY.
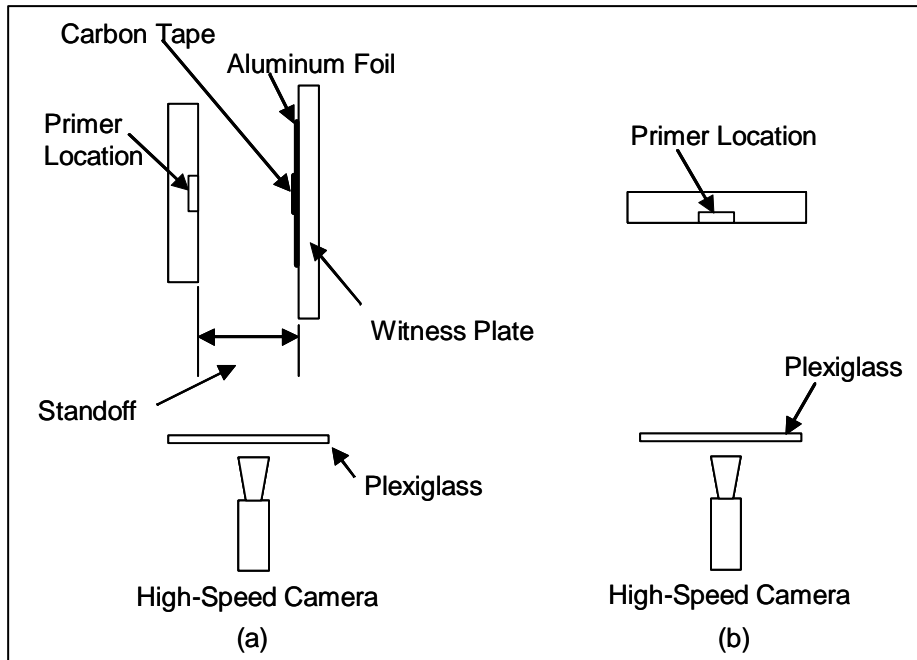
Figure 2. Experimental setup for high-speed video of primer output viewed
(a) perpendicular to line-of-sight (LOS), open-air/witness plate, and (b)
parallel to LOS, open air.

All open-air experiments were conducted at ambient temperature and pressure.

2.2 Ballistic Simulator Experiments

Figure 3 depicts a schematic drawing of the ballistic simulator used in the present work. The simulator consisted of a 25.4-mm (1-in) outer-diameter acrylic cylinder which was machined to approximate the geometry and volume of the 5.56-mm cartridge. The tapered walls in the 5.56-mm cartridge were not reproduced in the simulated chamber. Given the small size of the 5.56-mm cartridge chamber and the short duration of the ballistic event it was believed that the omission of the taper was not significant for the purpose of this study. The simulator chamber volume available to propellant was 1.52 cm³ (0.093 in³).
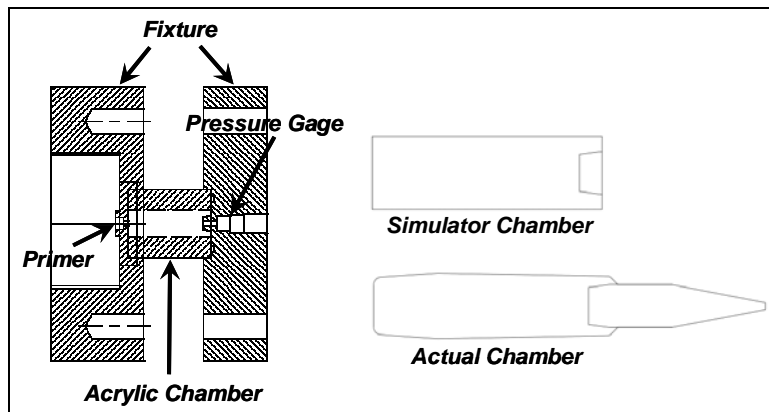
Figure 3. Schematic drawing of the 5.56-mm ballistic simulator.

4

Noting figure 3, the simulator chamber was sealed on both ends by steel plates, which comprise the experimental fixture. The plate located on the primer end of the chamber was the same plate used in the previously mentioned open-air primer experiments. The primer end plate included a right cylindrical hole (diameter = 2.03 mm [0.080 in]; depth = 1.65 mm [0.065 in]) through which the primer vents.

The steel plate located on the forward end of the chamber was machined to simulate the intrusion of the projectile. The projectile was fixed and not permitted to move relative to the chamber. A central hole was drilled in the simulated projectile and forward plate to accommodate a Kistler 211 B1 pressure transducer. Chamber pressures were acquired at a 1-MHz sampling rate.

Grooves were machined into the steel plate surfaces, where the plates were in contact with the ends of the acrylic chamber, so that o-rings could be used to seal the steel plates to the ends of the acrylic chamber. The plates were fastened together with four bolts.

Variants of the ballistic simulator experiments included a chamber that was empty or filled with inert or live propellant. The propellant used in the 5.56-mm ammunition, known as WC844, is pancake shaped and has a nominal diameter of 0.6 mm. The inert propellant chosen for these experiments was 0.8-mm-diameter Teflon spheres. Figure 4 shows the inert and live propellants used in the experiments. It is apparent from the figure that the Teflon spheres are more uniform in shape and will have a lower (compared to that of the actual propellant) volumetric loading density. Figure 5 is a photograph of the ballistic simulator loaded with the Teflon spheres.
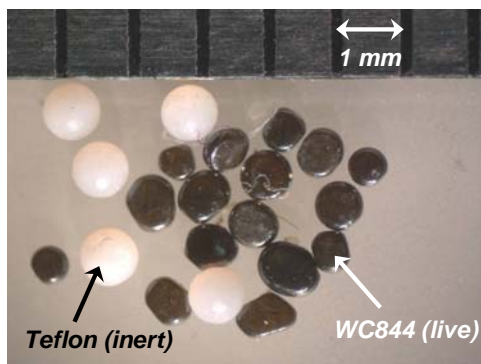
Figure 4. Photograph of inert (teflon) and
live (WC844) propellant used in
simulator.

Both the inert and live propellants were loaded into the simulator chamber by setting the chamber vertically on the projectile end plate. The propellant was then poured into the chamber until it was flush with the opposing end. The chamber was in no way vibrated to settle the propellant or increase the loading density. The average propellant mass for the two inert simulator tests was 1.85 g. The Teflon density (*10*) was 2.16 g/cm^3 and the average volume occupied by the inert spheres was 0.86 cm^3 (57% of the chamber volume), the average live propellant mass for the two live simulator tests was 1.54 g. And given the WC844 propellant
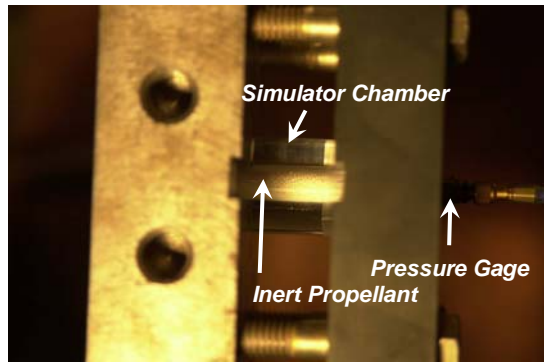
Figure 5. Small-caliber simulator with inert
propellant.

density (*11*) of 1.547 g/cm^3 the average volume occupied by the live propellant was 1.00 cm^3 (66% of the chamber volume).

For all of the simulator experiments, high-speed digital video was recorded of the flamespreading event. A Phantom V5.0 high speed camera, fitted with a 200-mm zoom lens, was employed to record the visible light as it propagated through the chamber. The camera was set to a frame rate of 3800 fps with an exposure of 16 µs (resolution 256×64).

A solenoid was utilized to drive a firing pin which initiated the primer. The time required for the solenoid to energize and cause the firing pin to strike the primer was not reproducible. As a result the absolute times reported for the pressure measurements during different tests are not comparable.

All simulator experiments were conducted at ambient temperature and pressure.

2.3   Full-Scale Gun Firing Experiments

Figure 6 schematically illustrates the gun firing fixture. The gun fixture was fitted with three pressure gages. A Kistler 607C4 piezoelectric gage and a Minihat strain gage were located axially in the middle of the gun chamber (20.1 mm from the primer end of the cartridge). The third gage, a Minihat strain gage, was located 46.8 mm from the primer end of the cartridge. This location corresponds to the case mouth. The case mouth pressure gage is exposed to the gas pressures behind the projectile only after the projectile has moved forward and cleared this gage. The gun tube was rifled and has a 1 in 12 twist and 457 mm of travel. The pressure-time data were recorded at a 1-MHz sampling rate.

New unprimed cases were drilled to accommodate the pressure gages. The case holes were sealed with tape. New primers were then attached to the case. The propellant was removed from a standard 5.56-mm round (lot LC05), weighed, and loaded into the drilled case. New projectiles were then weighed and crimped to the case. The projectile and propellant masses averaged 4.04 and 1.78 g, respectively. All components of the test rounds were provided by the 5.56-mm ammunition manufacturer, the ATK Lake City Army Ammunition Plant.
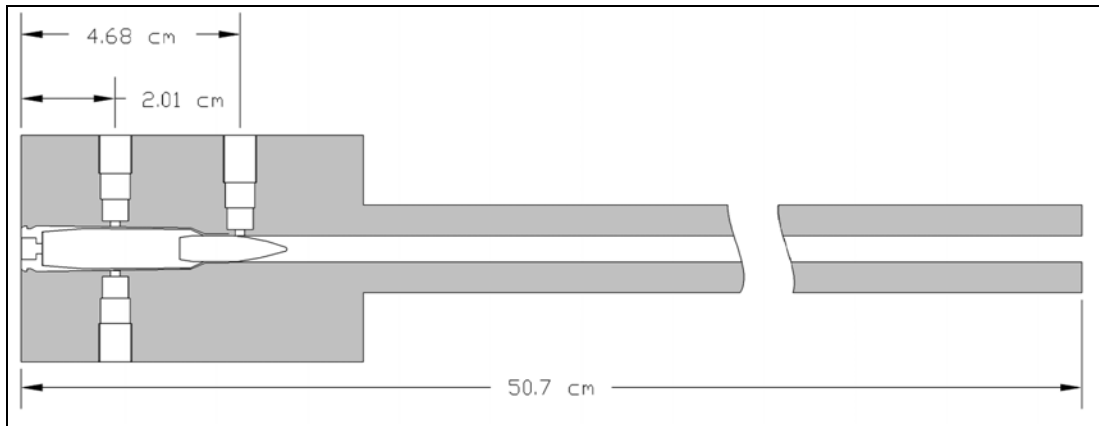
Figure 6. Schematic of gun firing fixture.

The projectile muzzle velocity was measured using Oehler Research, Model 55 light screens. The light screens were used to measure the velocity by recording the time elapsed between the time the projectile crosses through the first and second light screen. The first light screen was located 63 cm from the end of the gun tube and the screens were separated by 34.35 cm.

Projectile motion and velocity were recorded using a Terma Elektronik IM 400-55 (55 GHz) radar. This technique has been shown to be effective in recording in-bore projectile motion (*12*, *13*). The radar signal was reflected down the gun tube to record in-bore projectile motion and velocity as a function of the projectile position. The radar data were recorded at a 25-MHz sampling rate.

3.   Experimental Results and Discussion

3.1   High-Speed Photos of Primer Venting Into Open Air

The first series of tests was conducted in which the primer was initiated and vented into open air through a 2.03-mm-diameter vent hole. Figure 7 shows the open-air primer output for test 020. The camera settings for test 020 were 22000 fps and an exposure of 35 µs. The shock structure is established quickly and appears strongest and most well-defined at about 90 µs (measured from the time visible light first appears). The approximate locations of the precursor shock and the mach disk are noted in figure 7 (90-µs frame). From the first two video frames (first light to 45 µs), it can be estimated that the precursor shock initially propagates at about 475 m/s. Supersonic flow is, at this point in time, necessarily present behind the Mach disk (nearest to the primer). The high speed of the venting primer gases is not, however, maintained and the shock structure quickly deteriorates as evidenced by the subsequent photos in figure 7.

Figure 8 (test 022) depicts a similar primer initiation event as that shown in figure 7 (test 020). However, the photos taken during test 022 are recorded from the view illustrated in figure 2b (viewed along the center line of the primer flow as the primer vents toward the camera). The

7
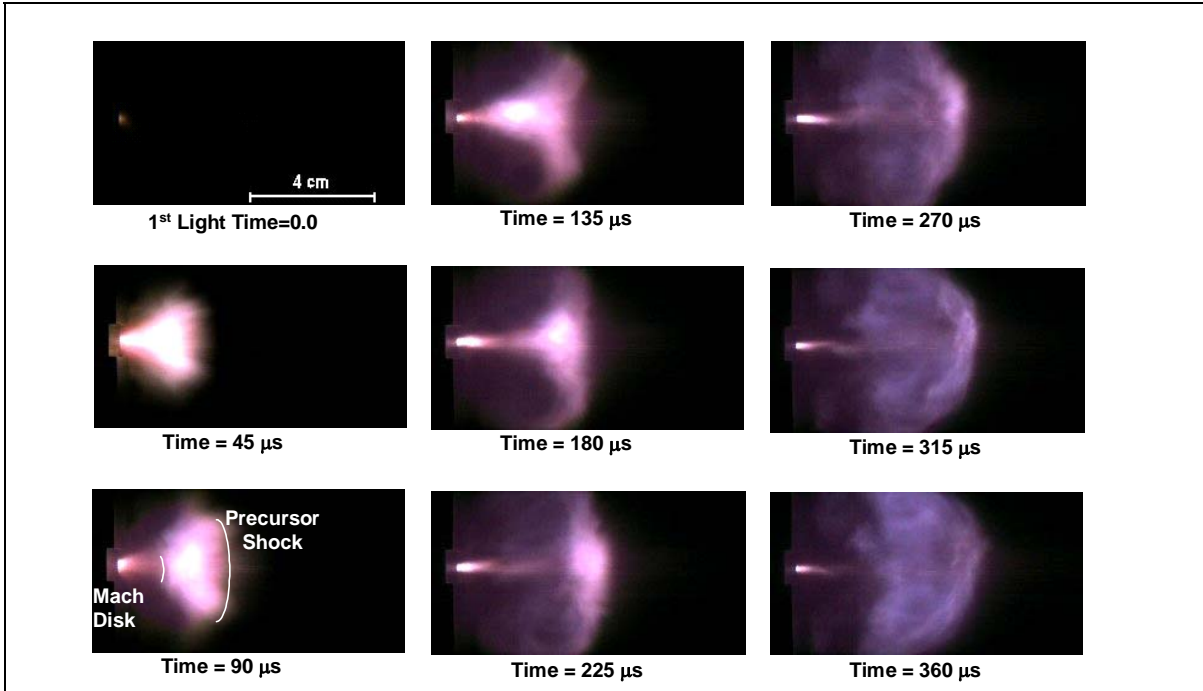
Figure 7. High-speed video of primer output (frame rate = 22,000 fps, exposure = 35 µs [test 020]).
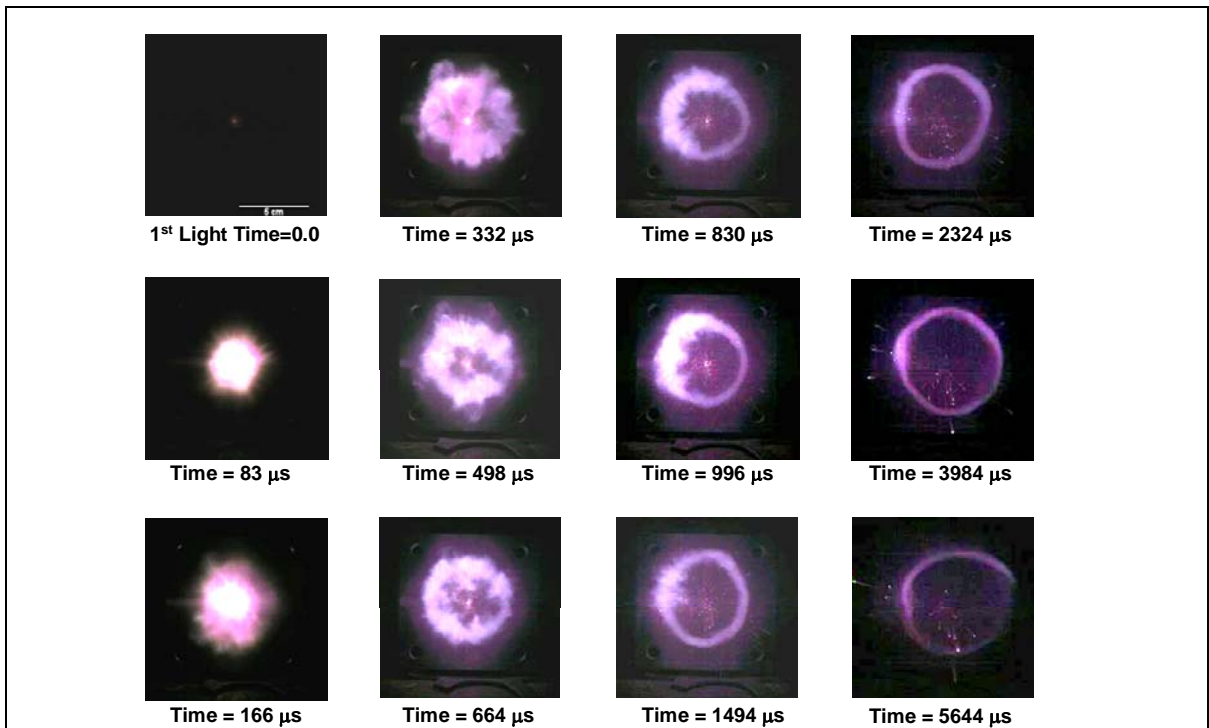
Figure 8. High-speed video of primer output-end view (frame rate = 12,000 fps, exposure = 73 µs [test 022]).

video images from test 022 were recorded at a frame rate of 12000 fps with an exposure of 73 µs. In the photo labeled 83 µs (measured from first visible light) there is seen an end view of the strongest shock structure (noting this occurs at a similar time as the 90-µs photo in figure 7). The visible light from the primer appears generally symmetrical as would be expected. As time elapses, the precursor shock is seen to form a ring (at times greater than 1 ms).

The digital photos captured for test 018, shown in figure 9, were recorded with a longer exposure time (110 µs) and a lower frame rate (7400 fps) in an effort to provide additional light to observe more of the particles venting from the primer. The particles appear to be accelerating ahead of the precursor shock (time = 405 µs in figure 9, for example) and are visible well after 1.2 ms.
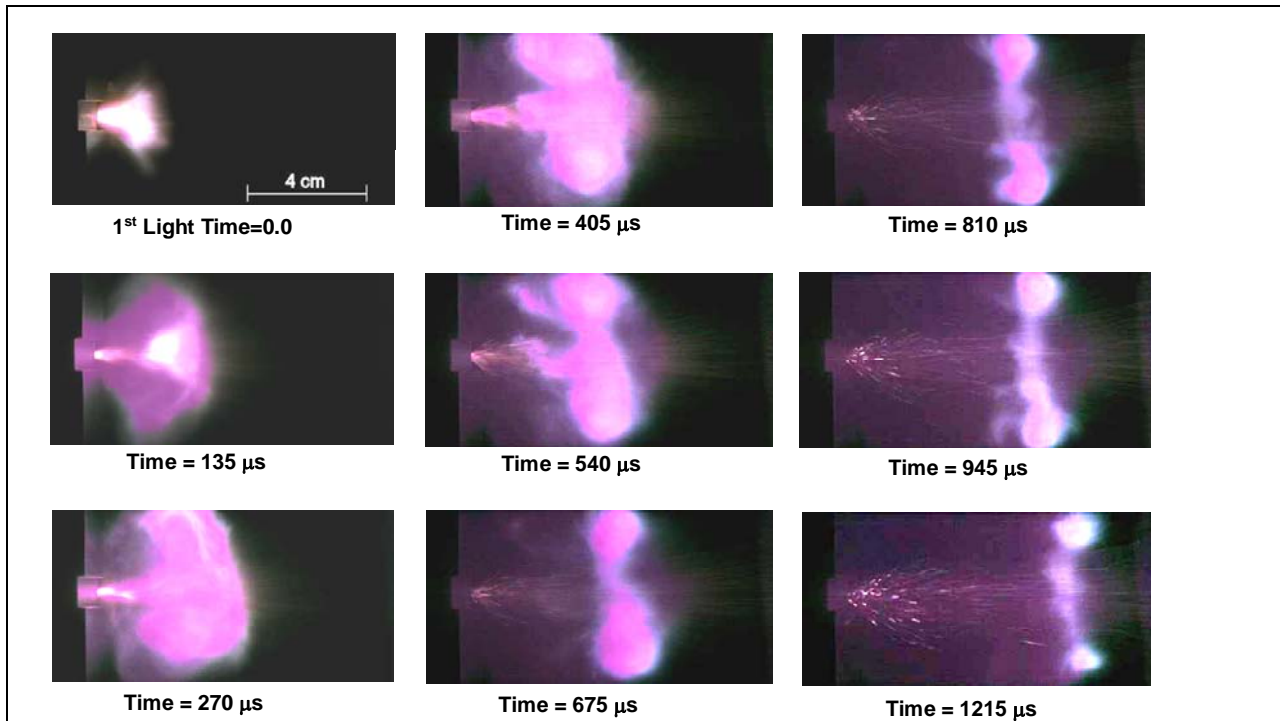
Figure 9. High-speed video of primer output (frame rate = 7400 fps, exposure = 110 µs [test 018]).

The particles accelerating ahead of the precursor shock are relatively small (compared to the later arriving particles venting from the primer, well behind the precursor shock). From the test 020 photos (figure 7), an average velocity of a random selection of these small particles (ahead of the precursor shock) was calculated to be 300 m/s early in the primer venting event (between 90 µs and 180 µs). Further tracking of the smaller particles reveals their velocities to be dropping quickly as would be expected.

Brighter and larger particles are more evident venting from the primer after about 1/2 ms has elapsed from first light (see figure 9). In the time space near 500 µs, the velocity of a random selection of particles exiting the primer was averaged to be 45 m/s. Still later (1.2 ms after first light), the largest particles visible were measured to have an average velocity of 15 m/s. The

particle velocities were calculated assuming the subject particles are moving parallel to a vertical plane passing through the primer center axis.

The shock structure seen in figures 7–9 is consistent with the general understanding of supersonic flow. Figure 10 shows a schematic of the gas dynamic features expected in highly underexpanded supersonic jets (*14*).
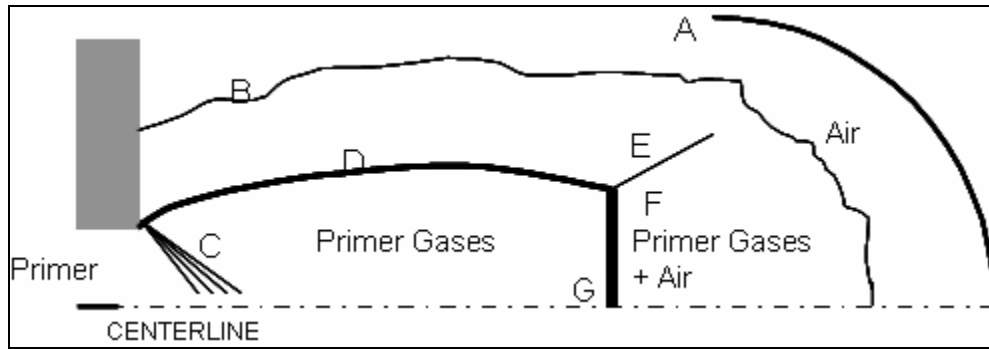
Figure 10. Schematic of gas dynamic features in a highly underexpanded jet (see text for label description).

The efflux of plasma from the capillary generates a precursor shock (A) that expands spherically. Behind this shock is air; the plasma is entirely contained by this shock and is separated from the air by an irregularly shaped contact surface (B) across which pressure and velocity are preserved but entropy changes discontinuously. Expansion waves (Mach cone), generated at the capillary exit (C), travel to the precursor shock (A), are reflected as weak compression waves, and coalesce into a strong oblique shock, or barrel shock (D), within the plasma jet. This barrel shock (D) terminates in an irregular reflection that forms a triple-point (E) joining the barrel shock (D) its reflection (F), and a normal shock (G) or Mach disk. Whereas the precursor shock (A) is relatively weak and diffuse, producing a mildly supersonic flow, the barrel shock (D) and Mach disk (G) are strong shocks that enclose a fully supersonic flow region (*14*).

Nusca's modeling predictions highlight the detailed gas dynamic features for a plasma venting into air and these features are applicable to the venting primer gases discussed here (*14*).

Clearly all of the shock structure details are not visible in figures 7–9. This is likely due, in part, to camera saturation by the visible primer light. The use of neutral density filters could be introduced if the shock structure details were of additional interest.

The diameter of the vent hole in the primer experimental fixture, through which the primer vented, was monitored throughout these experiments. The hardware was made of 4340 steel. A

total of 30 primers were fired with this hardware and there was no measurable (<0.001 in) change in diameter.

3.2   Witness Plate Observations for Primer Output

Additional experiments were conducted in which an aluminum plate covered by commercially available aluminum foil was placed in the path of the primer output. Figure 11 shows the aluminum foil witness plates which were located 66.5 and 123.5 mm from the primer source for test 025 and test 026, respectively. The highest concentration of indentations on the aluminum foil was located within a circle measuring about 70 mm in diameter. As would be expected, the particle density was noticeably greater for the witness plate located closest to the primer. The aluminum foil witness plate also indicated a relatively small number of particles were present outside the primer-fan (the area generally seen [in the digital video] to include the primer flow). High-speed flow containing both gas and particles has been shown to propel particles outside the nominal geometry of the flow (15). It can also be seen at later times (1215-µs frame, figure 9, for example) that a portion of the larger and slower particles are exiting the primer at greater angles than those of the smaller faster particles.
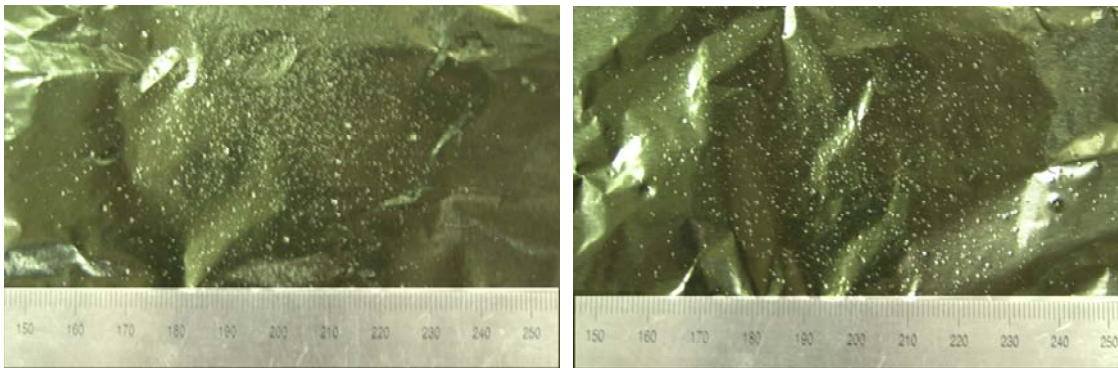
Figure 11. Aluminum foil witness plates located 66.5 (left) and 123.5 mm (right) from the primer.

Tests 029 and 030 were conducted with double-stick carbon tape (diameter = 25.4 mm [1 in], thickness = 1/4 mm) placed in the center of the primer flow at distances of 66.5 and 123.5 mm, respectively. Figures 12 and 13 depict photographs of the particle laden tape post firing. Similar to figure 11, it can be seen that the greatest particle density is present on the experiment on which the standoff distance was 66.5 mm. The particle pattern appears generally uniform and symmetrical.

3.3   Particle Analysis

The residue from open-air firings was collected on adhesive tape and analyzed using a Hitachi 4700 field emission scanning electron microscope (FE-SEM). Images were obtained with a secondary electron detector, and the energy dispersive spectra were obtained with an energy dispersive x-ray analysis (EDAX) detector. Residue was also obtained by capturing material on Teflon balls placed in the chamber during the firing. Infrared microreflectance spectroscopy,

Figure 12. Particles on carbon tape/disk witness plates located 66.5 (left)
and 123.5 mm (right) from the primer (disk diameter =
25.4 mm [1 in]).
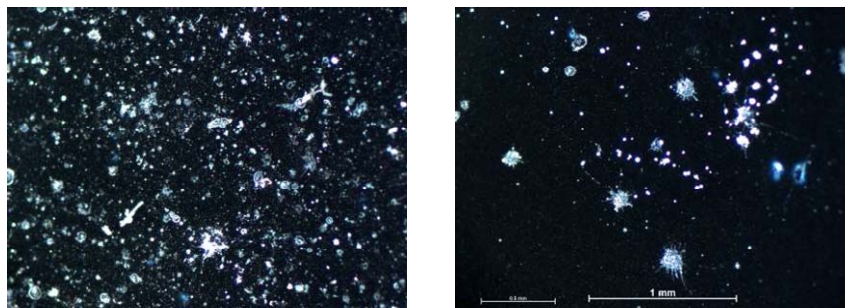
Figure 13. Particles on carbon tape/disk witness plates located 66.5 (left) and
123.5 mm (right) from the primer (magnified).

using a Thermo-Nicolet 870 Nexus Fourier transform infrared (FTIR) spectrometer with a Continuum microscope, was used to analyze residual material. Library spectra were obtained using Bio-Rad Infometrics "Know-It-All" software.

The main components of medium-caliber primers are lead styphnate, barium nitrate, and antimony sulfide, Sb_2S_3. Lesser amounts of aluminum powder, tetracene, and pentaerythritoltetranitrate (PETN) are also normally present. Additionally, cellulose and shellac may be used to help seal the composition.

The primer residue consists of many inorganic particles and some fibers from cellulosic material which is added to the primer (figure 14). At higher magnification (figure 15), particles can be observed having an irregular shape and surface, suggesting that those did not melt. Other particles appear quite spherical and smooth, quite probably because they had melted. Still others appear as though they had definitely melted, but had splattered upon impact with the adhesive-covered medium. At higher magnification (150–2500×) (figure 15), it is quite apparent that some much smaller particles (~1 µm) are present and are spread over the main particle in the image.
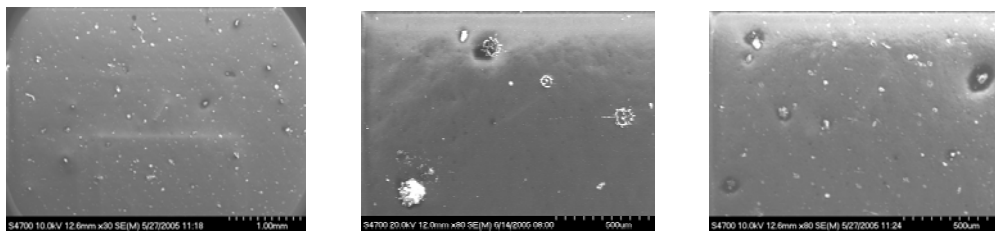
Figure 14. Low magnitude FE-SEM analysis of particles collected on adhesive tape from open-air firings. Many particles are on the order of tens of micrometers and are readily observed at low magnitude.

(a)	(b)	(c)
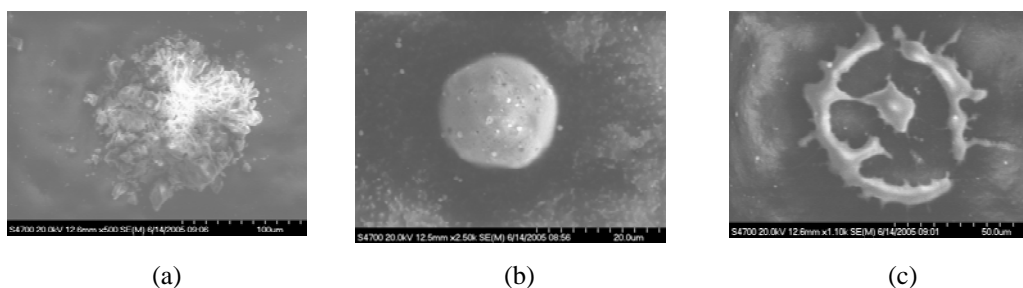
Figure 15. FE-SEM images (150–2500 $\times$ magnification) of three different types of particle morphology. Particle "a" apparently did not melt, while particle "c" apparently was melted when it hit and splattered. Particle "b" probably did not melt since it has so many Al particles coating it.

In addition to imaging the particles, EDS spectra were also obtained. Many particles were analyzed, and some representative results are shown in figures 16–20. EDS analysis is particularly useful for identifying elements but does not provide information about which elements are bonded together. EDS is not the most reliable method for assessing the levels of light elements, such as carbon, oxygen, and nitrogen in a sample. Our intention was to survey the morphology of the residual particles and to understand the distribution of the elements such as Al, S, Sb, Ba, and Pb in these particles. In this work, vibrational analysis was used to identify residual compounds containing these elements. The EDS spectrum in figure 16 shows that the main inorganic element present in the unmelted particle is barium. The EDS spectrum in figure 17 shows that the melted particle contains largely barium, but also contains Sb and S. Figure 18 shows that the nearly spherical particle contains primarily Sb and S, but with Ba also present. Additionally, this particle is coated with many tiny particles. Figure 19 is an EDS spectrum for which the focus was primarily on one of the tiny particles. The large growth of Al in the spectrum shows that the tiny particle is Al. Small particles ranging from about 0.1 to 10 µm were ubiquitously dispersed over the samples (e.g., the bright spots in figure 20, which also yielded the Al spectrum).

13
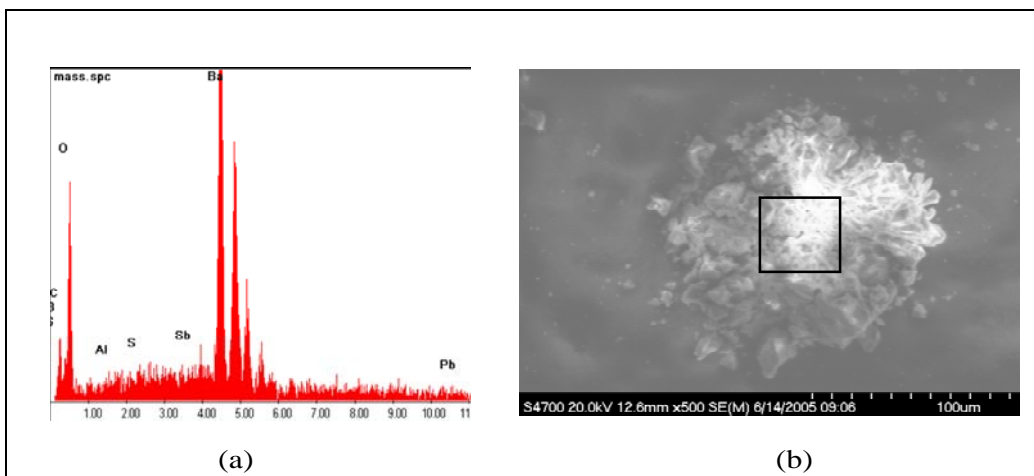
Figure 16. (a) EDS spectrum of blocked area of (b) particle showing that this particle, which apparently did not melt, consists primarily of Barium.
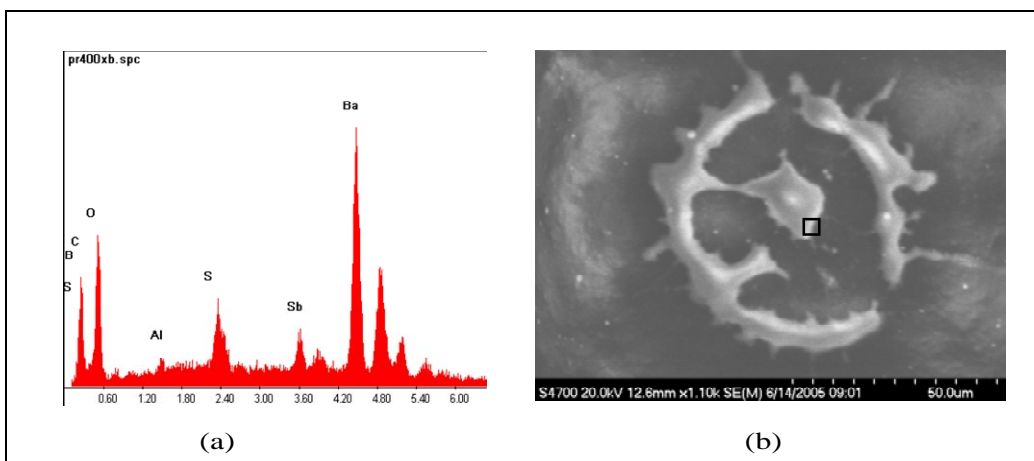
Figure 17. (a) EDS spectrum of the area indicated by the square in (b) the dispersed particle. This particle contains Ba, but with Sb and S also present.
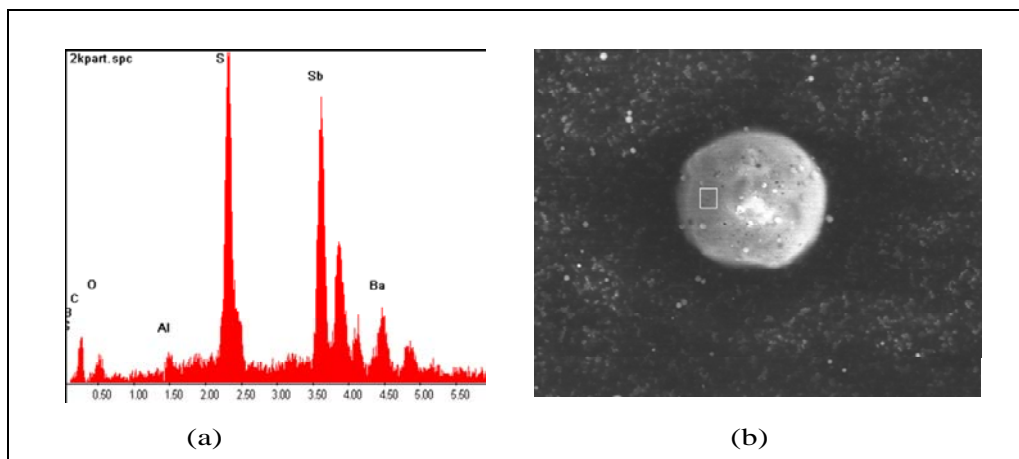
Figure 18. (a) EDS spectrum of the area indicated by the square in (b) particle. This particle contains mainly Sb and S, with Ba also present.

14
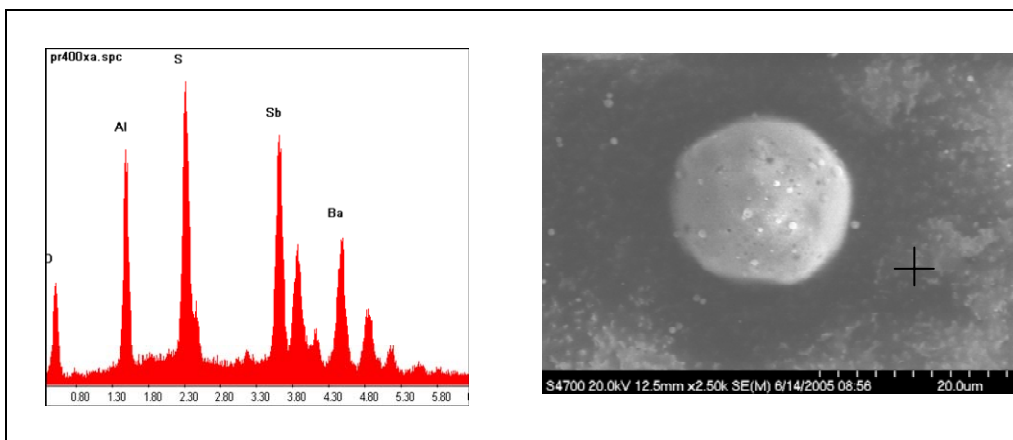
Figure 19. Tiny Al (~1–10 µm) particles (crosshair) are superimposed on the main particle.
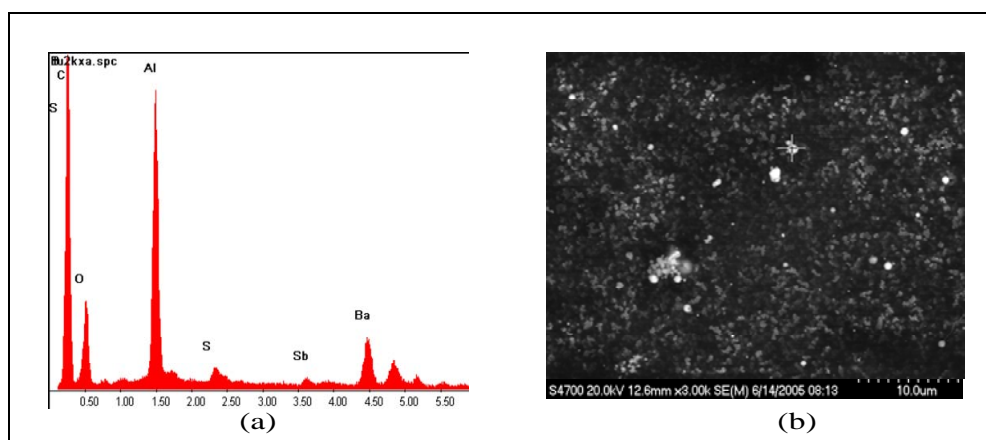
Figure 20. (a) EDS spectrum of one of the very small Al particles which coat all areas of
(b) the sample.

It should be noted that in obtaining the EDS spectra, various areas of the particle were sampled. The elemental analyses were consistent over the entire particle. The only exception is that if the area contained the small aluminum particles, then aluminum would of course be present in the EDS spectra.

3.4   Infrared Analysis-Analysis of Primer Stubs From Open-Air Analysis

Particles collected onto adhesive stubs were fired under open-air conditions. Infrared microspectroscopy was done directly on particles adhering to the primer stubs. A reference sample of adhesive was obtained, but normally interference by the adhesive compound did not prohibit interpretation of the spectra of the particles. In some cases, the particles were large enough to correlate with the images obtained in the SEM. In particular, the larger particles of barium are identifiable in the 15× objective of the FTIR microscope, either as having been melted ("splattered" or "wheel" shapes) or the more compact but still relatively large, roughly spherical albeit irregular, shapes.

15

FTIR analysis of the particles after open-air firings showed that nitrate was found in most of the particles examined. Nitrate was found in all of the larger particles containing barium (figure 21). At first, this was somewhat surprising. Our prior experience has been with characterization of energetic organic nitrate esters, such as nitrocellulose, and the gelling agents or plasticizers nitroglycerin and diethyleneglycol dinitrate (DEGDN). In interrupted burning rate experiments in which the propellant is extinguished at low pressure shortly after initiation (and for which most material is unconsumed), the decomposition product formed by the denitration of the nitrate ester functional groups is the carbonyl, and in those samples it is virtually ubiquitous. It does not take high temperature or long exposures for denitration of organic nitrates to occur. So it was assumed nitrate from inorganic barium nitrate would also decompose readily.
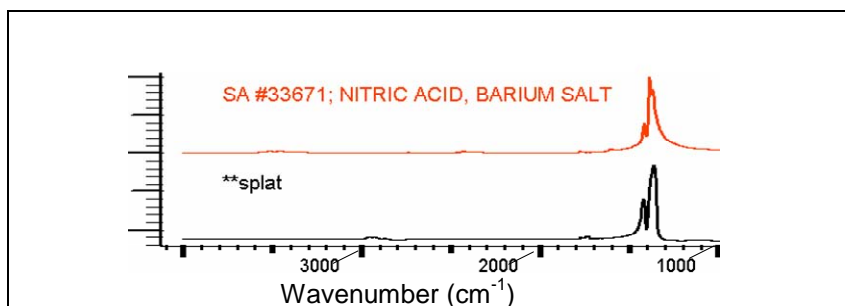
Figure 21. Reference spectrum of barium nitrate (top) compared to a spectrum representative (**splat) of many residual particles from open-air firings. The y-axis is in units of relative intensity, and the main absorbance bands are at 1420 cm^{-1} and 1390 cm^{-1}.

However, it was found that the nitrate remained even in barium samples which had melted. Some investigation into the properties of the Group 2 elements explained this. Barium nitrate, like all the Group 2 elements (Be, Mg, Ca, Sr, Ba, and Ra, in increasing size, respectively) undergoes thermal decomposition to give the metal oxide, nitrogen dioxide, and oxygen.

Thus, if "X" represents any one of the elements:

$$2X(NO_3)_{2(s)} \longrightarrow 2XO_{(s)} + 4NO_{2(g)} + O_{2(g)}.$$

With increasing size, the nitrates are more stable and must be heated more strongly before they will decompose (*16*). Since Ba, with an atomic number of 56, is the second largest in the series, its nitrate is relatively thermally stable and was readily detected in all of the residual barium particles from the open-air firings that were analyzed by FTIR. It is possible that some of the barium nitrate decomposed, but the only residual would have been BaO, which would not have been detected.

Decomposition products of other species were detected. At 15× magnification, particles were present that could be differentiated from barium particles, appeared to be a light gray color, and yielded a spectrum that was a match for sulfate, presumably from the oxidation of antimony sulfide, Sb_2S_3 to $Sb_2(SO_4)_3$. Although a reference spectrum of antimony sulfate was not

available, several other sulfate reference spectra (e.g., Cu, Ca, Zn, and Mn) showed a peak centered at 1130 cm^{-1} (figure 22) that was an excellent match for the gray particle spectra. This gives evidence that antimony sulfide Sb_2S_3 oxidizes to antimony sulfate under the conditions of open-air firing. A band that may be due to the sulfite functional group was observed at 960 cm^{-1} (figure 23); no reports of an antimony sulfite compound were found, although sodium is quite common and could form a sulfite.
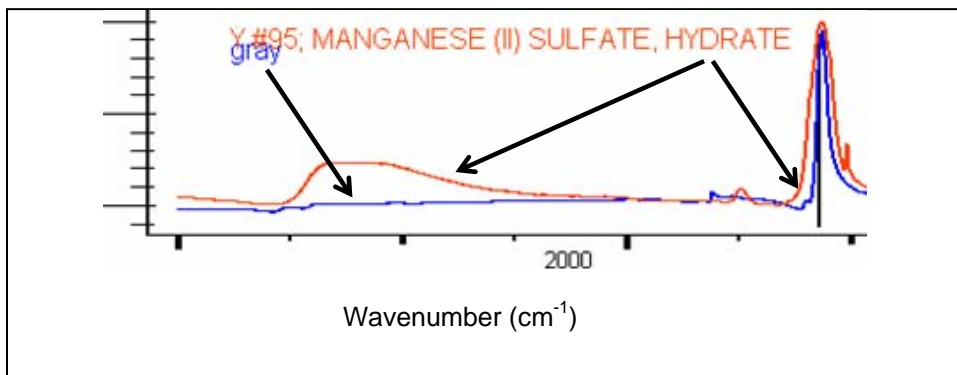
Figure 22. Reference spectrum of the hydrate of manganese sulfate, and a spectrum representative of several residual gray particles from open-air firings. The y-axis is in units of relative intensity, and the sulfate absorbance band is at 1130 cm^{-1}.
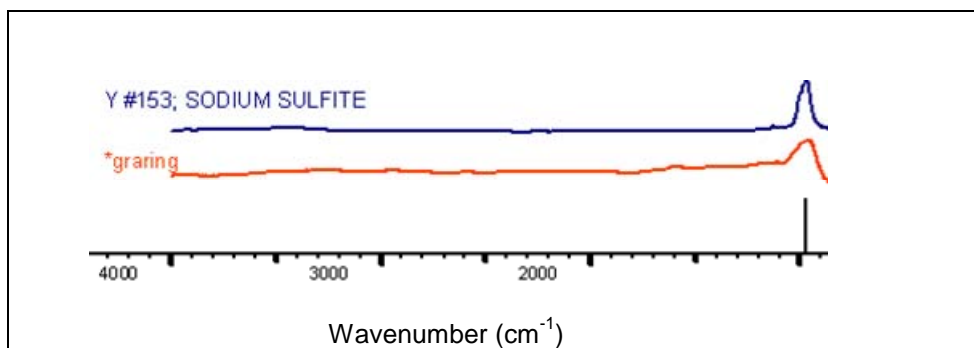
Figure 23. Reference spectrum of sodium sulfite, and a spectrum representative of a few residual gray particles from open-air firings. The y-axis is in units of relative intensity, and the sulfate absorbance band is at 960 cm^{-1}.

Thermochemical calculations, in which final equilibrium products are computed, predict antimony oxide as a final decomposition product. Antimony oxide has a strong 745-cm^{-1} absorption band, which should have been detected if a significant amount of the antimony existed in this form. It is noteworthy that lead styphnate has a distinctive infrared spectrum, which was not observed. Lead styphnate has an organic component, i.e., an aromatic ring containing hydroxyl and nitro groups, so it is quite possible that this decomposes more readily than the strictly inorganic compounds.

17

The melting points of typical inorganic primer components have a range of about 100 °C: Sb_2S_3, 550 °C; barium nitrate, 592 °C; and aluminum is a little higher at 660 °C. Aluminum is originally present in particles of the magnitude of tens of micrometers. The fact that tiny Al particles are found virtually everywhere suggests that, locally at least, temperatures greater than 660 °C are achieved. However, even though they have lower melting points than aluminum, not all the barium nitrate or antimony sulfide particles have melted. Since some do, they also must reach temperatures of at least ~600 °C. However, since not all the particles melt, there may be local regions where temperatures are lower, or not sustained sufficiently long to melt the particles, or both.

The thermal conductivity values for the primer components were not located, but values for the solid elements include (in W/cm∗K at 298 K), in increasing order: Ba, 0.184; Sb, 0.244; Pb, 0.353; and Al, 2.37. Thus, even though aluminum has the highest melting point of the primer components listed, it has a thermal conductivity that is probably at least an order of magnitude greater than the other materials. This may account for the fact that the very smallest particles observed are Al and that these particles are widely dispersed throughout the residue.

Another consideration is the overall primer composition (i.e., including the case). A typical commercially available 30-mm primer Material Safety Data Sheet (MSDS) shows that the primer consists of 80–90% by weight copper and zinc. The copper and zinc compose the primer case that holds the expelled particles that act as the initiating material. Assuming that the Cu and Zn exist as a brass alloy, the thermal conductivity (W/cm-K) would be between about 1.2 and 1.5. That is, the case has a much greater mass, and except for the Al particles, has a much greater thermal conductivity than the initiating particles. This allows the case to act as a huge heat sink, and it is conceivable that particles in close proximity to the case may be exposed to temperatures above their melting point, but perhaps not sufficiently long before the heat is transferred to the case and away from the particles. This may explain why some particles melt, while others do not.

It is interesting to note that in open-air firings, for which pressure levels are not expected to be as great as with closed chamber conditions (particularly when live propellant is used), the behavior of aluminum is quite different from other components. The SEM/EDS data show that particles other than aluminum have melted. Some particles of barium nitrate were captured in the process of budding into several smaller particles (figure 17b). Another particle that contained Sb, S, and some Ba had obviously been melted when it "splat" onto the adhesive tape (figure 24). But only the aluminum has dispersed into particles 1–2 orders of magnitude smaller in size than the original.
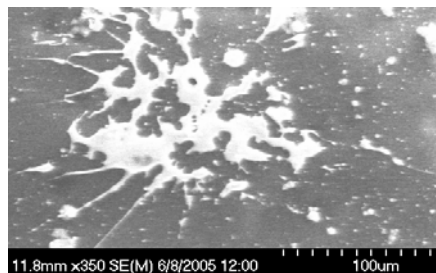
Figure 24. An FE-SEM image of a melted particle (containing Sb, S, and Ba; EDS spectrum not shown) that splat onto the carbon collection tape.

One might speculate that in order to achieve such a fine dispersion, the aluminum had burned. If the particles containing aluminum consist entirely of aluminum oxide, with no aluminum in the core, then that would support the idea of burning. The possibility is a melt process in which molten aluminum expanded thermally to crack the aluminum oxide layer. The molten aluminum could flow out, become oxidized, and form a smaller particle. Whether this could happen to the extent needed to form particles 1–2 orders of magnitude smaller than the original particle seems less likely, but is not totally dismissed at this time. Future work will include an assessment of whether the aluminum burns or simply melts, as the heat generated, and temperatures resulting from these processes, are much different. An estimate of the number and size distribution of the Al particles can be made based on the amount of material originally and the analysis of the material collected. The number, size, and temperature of the finely and uniformly dispersed aluminum particles are important to modeling the mechanism of propellant ignition.

Aside from aluminum, analyses of the other component particles give no indication that significant levels have burned in the open-air firings. As mentioned, other particles have not melted, and some particles (e.g., many barium nitrate particles) have not even decomposed. The situation for closed chamber firings can be quite different, and work is in progress to collect and analyze the primer products of firings with inert propellant in a closed chamber.

3.5   Analysis of Teflon Balls in the Chamber

Teflon balls were placed in the chamber as relatively inert materials onto which the residual material could be captured and depth profiled. The pressure achieved in these firings was 18.3 MPa (2350 psi) and was higher than those of the open-air firings. After the firings, the Teflon balls were removed incrementally by using tape to make the top layer of balls adhere. Those balls closest to the chamber were darkest, while further away from the chamber the balls appeared light gray. Metal deposits could be observed under low magnification (10–15×). The darkest, residue-rich balls were pooled separately from the lighter ones and provided for chemical characterization. Teflon is nonconductive and charges, particularly near the top surface, making SEM/EDAX analysis in a high vacuum system prohibitive (figure 25). FTIR analysis was then used.

19
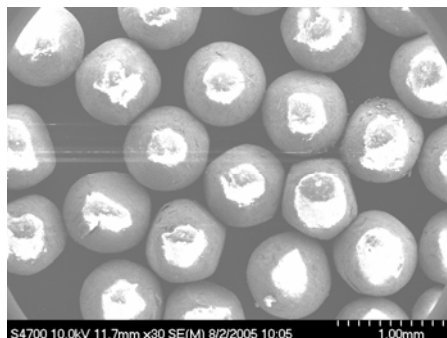
Figure 25. Teflon balls charge under high vacuum conditions, giving a "cream-puff" appearance.

Although there was significant residue observed, particularly on the darker balls, not many of the particles gave significant bands by FTIR analysis. Nitrate bands were observed from some particles, but these were not as prevalent as for the open-air firings. A Teflon substrate is not a major interference in FTIR analysis, since the C-F bonds are strong and sharp at ~1100 cm^{-1} and 1250 cm^{-1}, leaving an open window for analysis of most bands. Nonetheless, the only species observed was nitrate, although not as extensively as with the open-air primer experiments. The experimental and analyses set-ups allow for a semiquantitative interpretation of the results. In the open-air experiments, many particles were characterized, and nitrate was the most common species detected. In the Teflon ball set-up, most of the particles characterized did not yield an infrared spectrum. Thus, semiquantitatively, it appears that more decomposition or a greater extent of reaction occurs in the case of the Teflon ball firings.

It was also necessary to assure that the Teflon balls did not interfere physically from collecting a spectrum, for example by reflecting or scattering radiation. Removal of the sample from the balls would rule out this possibility. Initial attempts involved scraping the material, but recovery of the material was inefficient. Solvent removal was performed by sonicating the balls in methylene chloride, followed by removal of the solvent. The combination of mechanical removal and solvent extraction of the material proved to be very effective. This was done directly in shallow aluminum pans which could then be placed directly into the FTIR beam for analysis. After the solvent treatment the balls appeared pristine white, and a large amount of residue that looked rather sooty was obtained.

The infrared spectrum of the soot was "mapped" manually, and spectra with significant bands were saved. A few nice spectra were obtained, most likely from the grease used to seal the gages in place, the adhesive used to remove the balls for analysis, or residual Teflon (figure 26). There was not much to indicate that much CHON-containing species from the original primer composition remained. The fact that the grease and adhesive were found indicates that recovery of the material was effective.

20
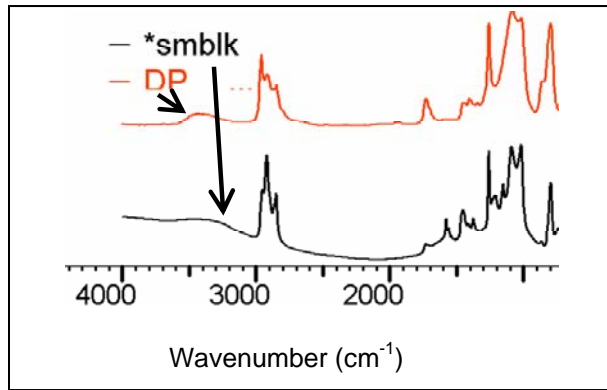
Figure 26. Spectrum of residue collected from the Teflon
balls (bottom spectrum), and a reference
spectrum of a viscous grease (top). The y-axis
is in units of relative absorbance.

4.   Ballistic Simulator Experiments

4.1   Empty Chamber

The empty ballistic simulator chamber quickly filled with visible light and the pressure rise was
expectedly abrupt. Figure 27 shows the empty chamber pressure response for the no. 41 primer
both filtered and unfiltered. The high frequency component of the pressure response (unfiltered)
is due to the complex interactions between multiple wave fronts reflecting between the two
chamber ends. The signal was passed through a 15-kHz low-pass filter in an effort to identify
and more clearly visualize the cyclic ringing of the pressure in the chamber. Four empty
chamber experiments were conducted, and the filtered (all 15-kHz low-pass) pressure-time
curves are presented in figure 28. The filtered versions of the data are presented only because
multiple unfiltered curves are more difficult to distinguish on a single plot. The chamber
pressure reaches its maximum value in 25–35 µs after the initial pressure rise. It is noted that the
empty chamber pressure-time histories are fairly reproducible and the average peak pressure
(filtered) is 3 MPa (435 psi).

4.2   Inert Propellant Chamber

The pressurization characteristics for the inert propellant bed are presented in figure 29 for two
separate experiments. The chamber pressures, which were reproducible, reached an average
peak of 18.3 MPa (2650 psi) in about 18–20 µs. The faster rise time (compared to that of the
empty chamber experiments) is expected since there is less volume available to the primer gases.
The acrylic chamber did not rupture but did have many stress cracks within the chamber wall.

21
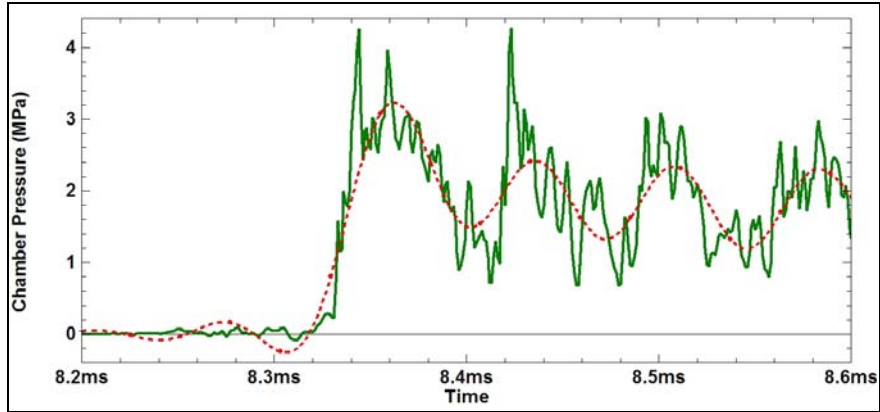
Figure 27. Pressure-time curves for empty simulator chamber (with and without 15-kHz low-pass filter).
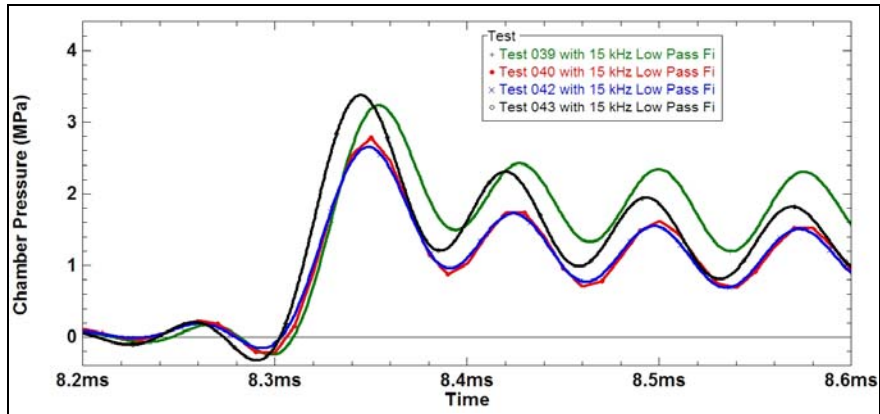
Figure 28. Pressure-time curves for four empty simulator chamber tests (with 15-kHz low-pass filter).
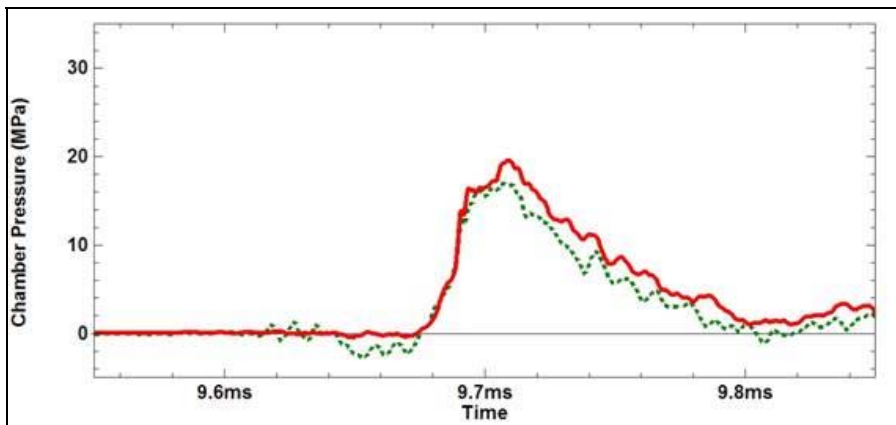
Figure 29. Pressure-time curves for two "inert" simulator chamber tests.

The pressure is then seen to decrease rather quickly. There was no evidence of leakage around the o-rings that sealed the chamber to the steel end plates.

Post firing analysis of the inert propellant bed included a visual inspection. The fixture plate located at the primer end of the chamber (with the chamber aligned upright) was removed. The first observation was that the propellant bed was no longer flush with the end of the chamber but was recessed about 1 mm. This suggests that the propellant bed had been compressed. The Teflon spheres were then systematically removed from the chamber and photographs were taken of the remaining spheres at various depths into the chamber. Figure 30 shows two photographs taken of the inert propellant. The first photograph (0 mm depth) was taken without removing any spheres. There is evidence of residual particles ejected from the primer (analysis discussed earlier) within the propellant bed. At a depth of about 14 mm, there first appears a distinguishable pattern on the spheres. The pattern is more pronounced at a 19-mm depth (see figure 30) where white circles are visible on the spheres. The darker region (outside the white circles) appears to be a carbon soot produced by the primer gases. The white circles grow larger in diameter as the depth into the chamber is increased indicating the spheres are more compacted in the forward area (opposite the primer). In the forward end of the chamber, the Teflon spheres were almost entirely white (minimal soot is present). This gives evidence to the primer effect of compacting the bed. At the 19-mm depth, it is also noticed that the visible presence of particles is significantly reduced and soon thereafter no particles are easily seen. The compaction of the bed greatly restricts the penetration of the primer gases. The propellant mass near the projectile effectively seems to act as a solid plug which would then press upon the projectile base.

0 mm depth   **19 mm depth**
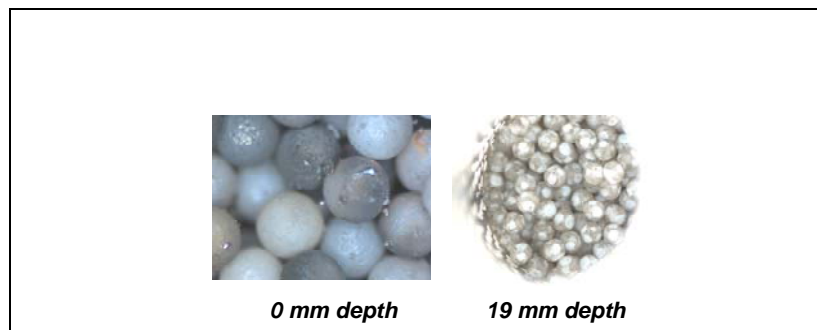
Figure 30. Photographs of post firing "inert" propellant in simulator chamber.

Stills from the high-speed video of the inert propellant simulator are shown in figure 31. The first frame shows a weak indication of the first light to appear. At 26 µs, the light appears the brightest. Given the time resolution the second frame is closest to the 18–20 µs point, at which the chamber reaches maximum pressure. At 52 µs, the light intensity has decreased but spread further into the chamber. Subsequent frames show the visible light steadily decreasing in intensity with slightly increased penetration into the propellant bed. The visible light appears to penetrate about 40% of the bed length (~12 mm).

Time = 0 (first light)   Time = 78 us

Time = 26 us   Time = 338 us

Time = 52 us   Time = 598 us
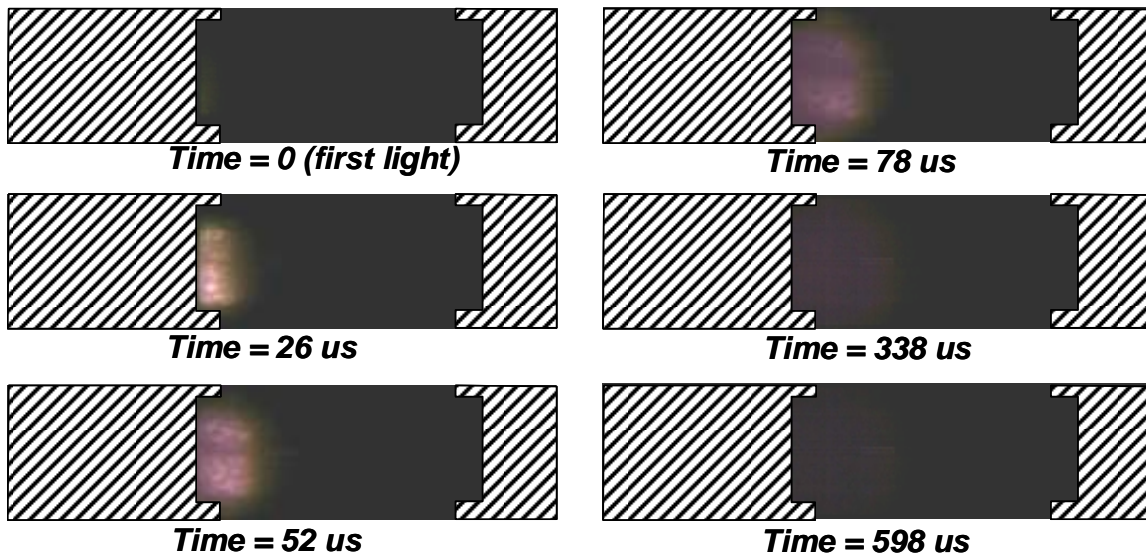
Figure 31. Flame spreading for inert propellant bed (test 046).

4.3   Live Propellant Chamber

Figure 32 shows the pressure-time histories for two separate tests with live WC844 propellant in the simulator chamber. The pressure curves again appear reproducible and have an average peak pressure of 30.2 MPa (4390 psi). At about 30 MPa, the simulator chamber ruptures and the pressure data in the figure are no longer valid.
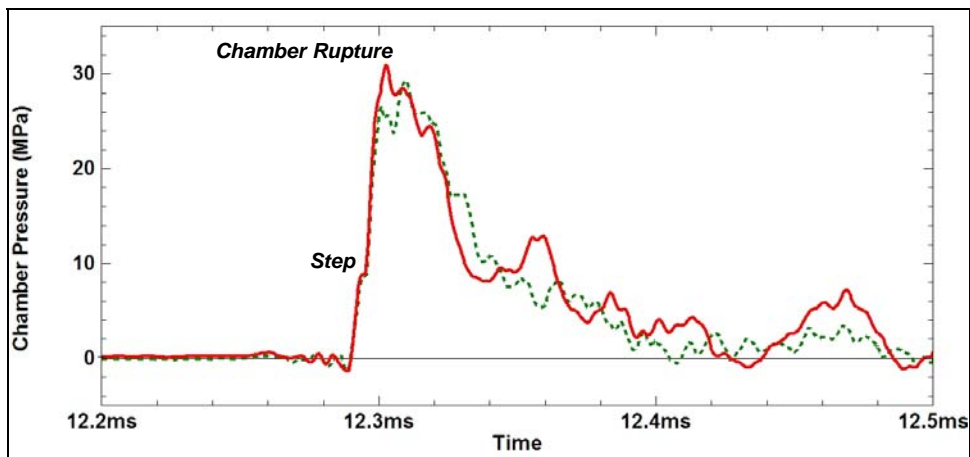
Figure 32. Pressure-time curves for two "live" simulator chamber tests.

There is a noticeable "step" at about 8 MPa in the initial pressure rise for the live simulator tests. This characteristic has been observed in other primer ignition studies and has been attributed to a choked to unchoked flow change as primer gases exit the primer (2). Further study may be needed to fully explore this possibility. The fact that the step is not as noticeable in the inert simulator is attributed to the difference in loading density.

24

The peak pressure is reached in about 10–12 µs, which is faster than the rise time for the inert simulator. This difference is highlighted in figure 33 where the change in scale makes the faster rise time more apparent. It is believed that the faster initial rise time is due to the increased volumetric loading density of the live propellant versus that of the inert propellant.
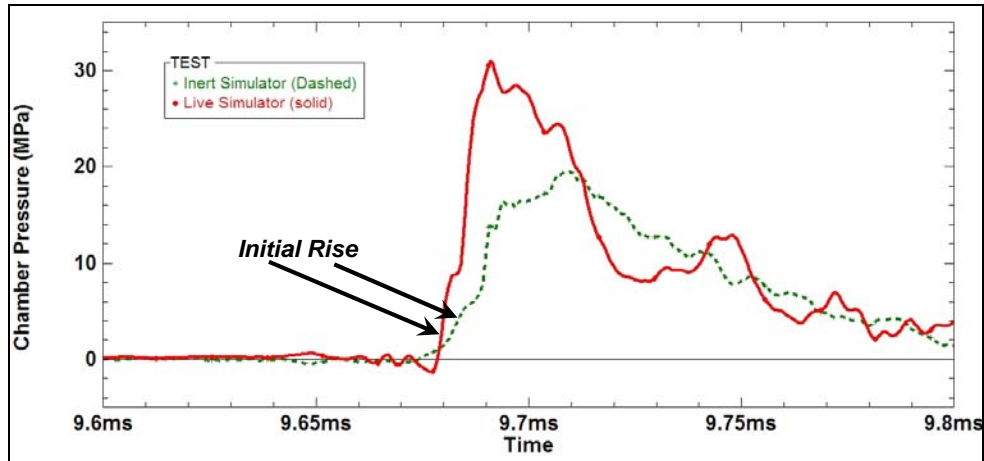
Figure 33. Live and inert simulator pressure-time traces.

The increased volumetric loading density is not, however, believed to be accountable for the large increase in peak pressure (30.2 MPa - live and 18.3 MPa - inert). As a first approximation from the ideal gas law (PV = constant), a pressure increase of about 5 MPa would be expected when considering only the change in loading densities. Instead, an increase of about 12 MPa is observed. The increase in peak chamber pressure is believed to be due to the ignition of the propellant. Further evidence of propellant ignition is apparent in the flamespreading photos shown in figure 34. At the time of 26 µs, after the appearance of first light, the visible flame appears the brightest. Further, the light is noticeably brighter than that seen in the inert simulator flamespreading photos (compare figure 31).

Visible light penetrates about 30% (~9 mm) of the length of the propellant bed, which is less than that seen in the inert experiments. As would be expected, the increased loading density appears to restrict the flame penetration. In the third frame (52 µs), there is evidence of the flame escaping above the initial chamber geometry. This indicates the chamber has already ruptured. The video evidence is consistent with the fact that the pressure-time curves peaked earlier (10–12 µs).
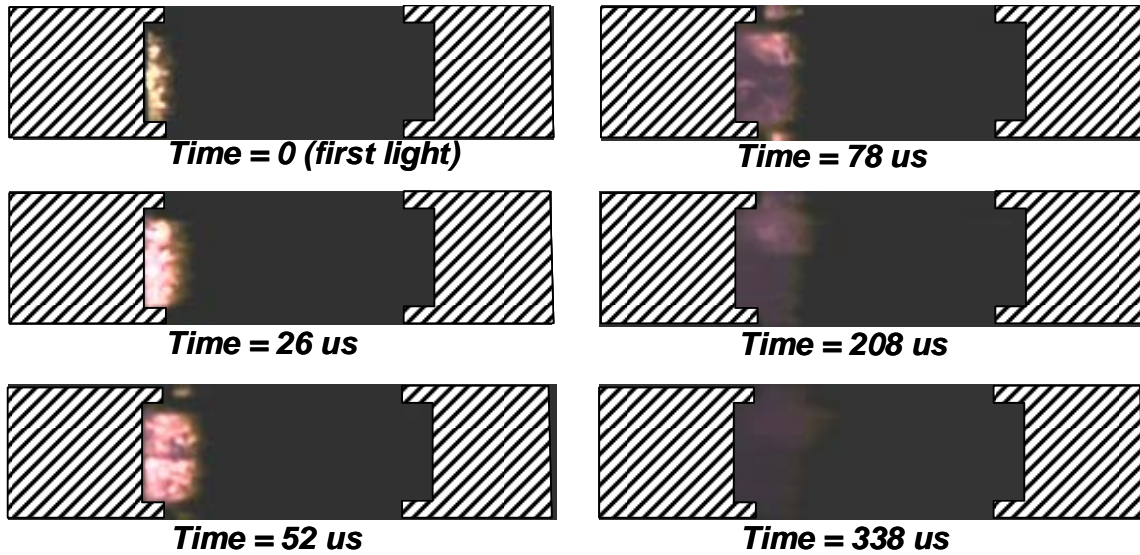
Figure 34. Flamespreading in live propellant bed (test 046).

5. Live Gun Firings

A series of gun firings were conducted to determine the best method of sealing (tape and glue options were investigated) the gage holes and crimping the case to the projectile in order to achieve advertised pressures (case mouth maximum pressure = 353 MPa [51.2 ksi]) and velocities (901 m/s [2956 fps] at 24 m [78 feet]) (*17*). Tests were conducted which produced similar case mouth pressures and velocities for drilled case rounds (crimped and uncrimped) and factory loaded rounds. Some drilled case rounds showed evidence of leakage around the gage holes. Such rounds, as would be expected, showed lower pressures. In general, crimping the round did not appear to increase the pressures, as might have been expected.

A representative drilled case round (test 065) is discussed here in detail. In figure 35, three pressure-time curves are plotted together for a full-scale gun firing. The curves have been shifted so that the initial pressure rise corresponds to time zero. P1 and P2 were recorded at the same axial location (20.1 mm from the rear face of the tube [RFT]) but with different gage types (a piezoelectric and strain gage, respectively). The different gages produced similar results. The peak pressures (360 and 366 MPa) were within 2% of each other. The case mouth gage (strain gage labeled P3, located 46.8 mm from RFT) recorded an initial pressure rise 320 μs after P1. The delay was due to the fact that the projectile had to travel about 10 mm before the case mouth pressure gage was exposed to the chamber gases. The peak case mouth pressure was 342 MPa, which is about 3% lower than a standard reference lot round (*17*). There was no visible evidence of leakage around the gage holes. The lower than expected pressure may be explained, in part, by the presence of the chamber gage holes. Port holes through which the gages measure the

chamber pressure increase the chamber volume. The port holes were filled with grease to protect the gages from heat and in an attempt to minimize this chamber volume effect. In large-caliber guns, the additional volume has been considered insignificant. However, the small-caliber chamber volume may be noticeably altered by the use of chamber gages.

Also apparent in figure 35 is the projectile exit time. Noted on the figure is the fact that both of the strain gages (P2 and P3) produced a bump in the curve at 1.102 ms. It is believed that the projectile exiting the muzzle produced a response through the gun which is recorded by the strain gages but not by the piezoelectric gage (P1).
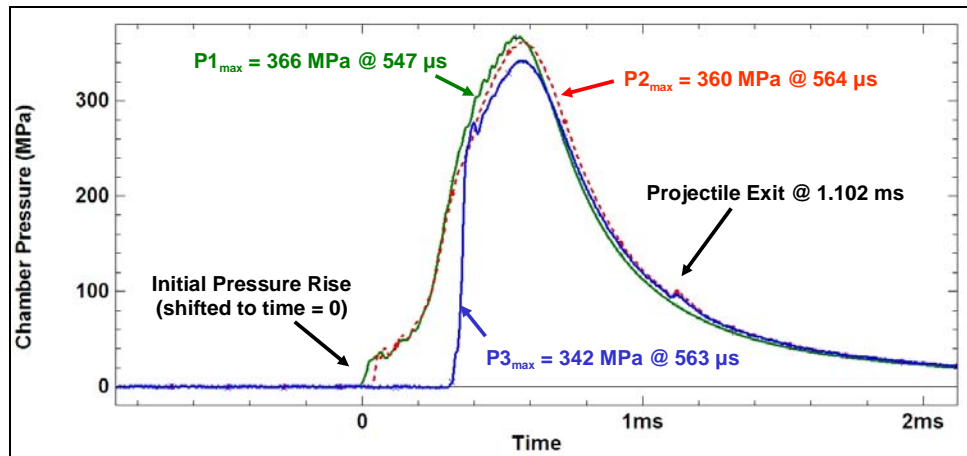
Figure 35. Pressure-time traces for small-caliber gun firing (test 065).

Figure 36 shows the pressure data (P1 and P3) along with the radar data for test 065. The initial rise (P1) is due to the primer output, which quickly pressurizes the chamber. The pressure begins to level off beginning at about 28 MPa (30 µs after the initial pressure rise). The leveling off of the pressure occurs over a time of about 100 µs (up to 130 µs) due to an increase in the chamber volume. The chamber volume is increased as a result of a combination of the brass cartridge case expanding and the projectile moving forward to engage the rifling (about 3 mm of travel). After the projectile reaches the origin of rifling, the slope in the pressure curve increases as the chamber volume is held constant momentarily. At about 130 µs, the pressure has reached 47 MPa and the radar data indicate the first noticeable movement of the projectile as it begins to travel down the rifled gun tube. At about 320 µs, the projectile has traveled about 10 mm, exposing the case mouth gage. At that time, the mid-chamber pressure is about 204 MPa.

Using the in-bore radar, the projectile muzzle velocity was measured at 908 m/s (2979 ft/s). Using the light screens, the muzzle velocity was recorded at 918 m/s (3012 ft/s). Employing a velocity retardation of 1.1 (m/s)/m, the projectile velocity is calculated to be 882 m/s and 892 m/s at 24 m (78 ft) for the radar and light screen measurements, respectively (*18*). The average measured velocity is about 2% lower than the reported velocity (at 24 m [78 ft]) for a standard M855 reference round (*17*).
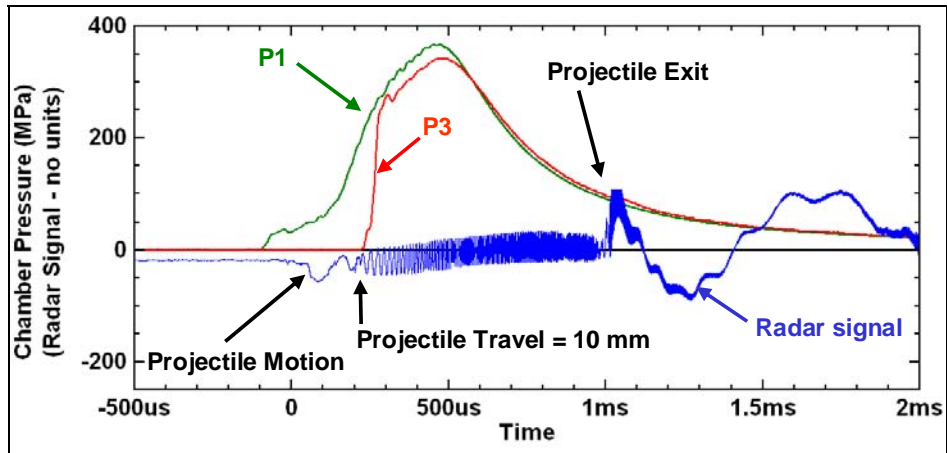
Figure 36. Pressure and radar data for small-caliber gun firing (test 065)

The measured peak case mouth pressure and projectile velocity were within the specifications of the instrumentation (less than 2% different than pressures/velocities for M855 reference rounds/data).

Early Pressurization Analysis

Figure 37 shows the first 150 µs (zeroed at the initial pressure rise for each curve) of the pressure data for the inert simulator, live simulator, and live gun firing. It is readily apparent that the initial slope of the gun firing pressure more closely tracks with that of the inert simulator than that of the live simulator. Table 1 presents additional details which help to explain the early pressurization characteristics.
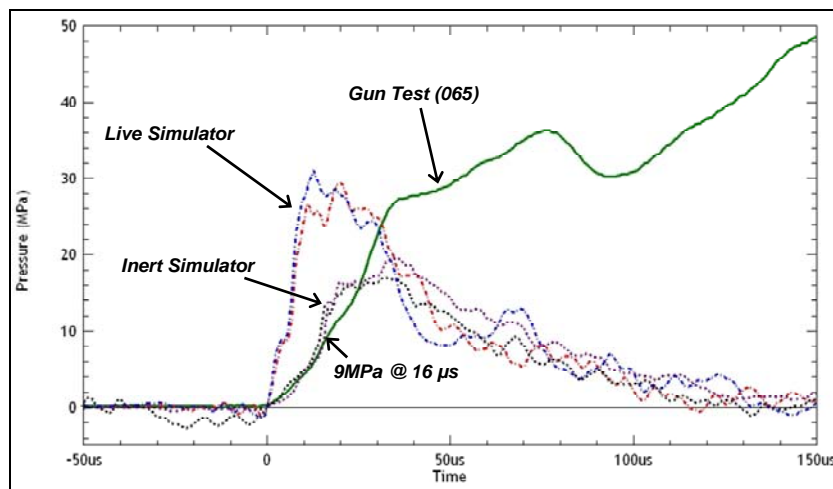
Figure 37. Pressure data for simulator and gun firing experiments.

28

Table 1. Comparison of case and simulator parameters.

	Charge Weight (g)	ρ (prop) (g/cm^3)	Vprop (cm^3)	Vcase/sim (cm^3)	Vfree (cm^3)	ρ (load) (g/cm^3)
New case	1.78	1.547	1.15	1.71	0.56	1.04
Fired case	1.78	1.547	1.15	1.78	0.63	1.00
Live simulator	1.54	1.547	1.00	1.52	0.52	1.01
Inert simulator	1.85	2.16	0.86	1.52	0.66	1.22

The table summarizes the loading details for the live and inert simulators and cartridge cases which are both new and previously fired. For each configuration, there is tabulated the propellant charge weight, propellant density, volume occupied by the propellant, volume of the case or simulator, free volume in the case (not occupied by the propellant), and the loading density. The previously fired case is of particular interest because it represents a true operating chamber volume. Assuming the brass case does not relax after firing, the case volume increases by about 4%.

From the table it can be seen that the free volume (Vfree) in the inert simulator more closely matched that of the actual fired cartridge and this would explain the similarity between the early inert simulator and gun firing pressure curves. While the propellant loading density for the live simulator (last column in the table) is nearly the same as that of the expanded case, the mismatch in initial free volume prevents the live simulator from capturing the initial slope details.

It is noted in figure 37 that at about 9 MPa the gun firing and inert simulator pressure curves begin to diverge. Since the simulator projectile is fixed, the divergence could be due to small projectile movement (increase in gun chamber volume). However, it is also possible that the simulator chamber and gun cartridge volumes are expanding to this point in pressure and the divergence signifies that the cartridge continues to expand while the simulator chamber does not. And later (~30 µs and ~28 MPa), when the gun pressure slope drops noticeably (signifying a larger change in chamber volume), the projectile has begun to move toward engaging with the rifling. The latter scenario seems more likely.

6. Summary

Open-air primer experiments have been conducted to characterize the output of the 5.56-mm ammunition primer (no. 41). The experiments have been designed to provide useful information for the development of a detailed model of the primer. The primer model is intended for use in a multiphase, multidimensional interior ballistics code. As a result, details of the energy delivered by the primer (convective, radiative, and through particles) are important.

Simulator and gun firing experiments have been conducted to better understand the ignition details of the small-caliber round. Specifically, the flame spreading and pressurization characteristics of the no. 41 primer have been investigated.

The simulator experiments reveal that the visible flame front produced by the primer penetrates about 30% and 40% of the live and inert propellant beds, respectively. The difference in penetration is attributed to the different loading densities.

The simulator grains show evidence of compaction near the projectile end of the chamber. There is clear evidence from the inert simulator data of compaction beginning about mid-chamber. Compacted grains are generally not a desirable result as this can impede gas flow in the propellant bed.

The propellant bed is locally ignited in the first 12 µs after the primer venting. Vigorous ignition of the propellant bed, however, appears to occur later (within 250 µs). Close analysis of the early chamber pressurization history revealed that the simulator chamber is a little smaller than the actual gun chamber. Part of this difference is due to the fact that the brass cartridge case expands (4% volume increase) during the ballistic event.

Projectile motion was correlated with pressurization of the gun chamber. The gun firing data indicated that the projectile begins to move into the gun tube at a pressure between 20 and 30 MPa. The early chamber pressure was shown to level off as a result of an increased chamber volume due to case expansion and the projectile moving forward to engage the rifling. Gun firing results produced pressures and muzzle velocities that were about 3% and 2% low, respectively. This may be due, in part, to changes in the chamber volume introduced by the use of pressure gages.

Using a variety of techniques and equipment (FE-SEM, EDAX, FTIR spectrometer), the particles produced by the primer (recovered from open-air and inert simulator experiments) were analyzed in detail. The data show differences in the residual particles including:

- Some particles of barium nitrate were captured in the process of dispersing into several smaller particles, while others did not melt.

- Some antimony sulfide particles remain intact, while in other cases the melted antimony sulfide "splat" onto the adhesive tape.

- Infrared analysis shows that much of the barium nitrate remains.

- Only aluminum has dispersed into particles (1 µm, some less), which are 1–2 orders of magnitude smaller in size than the original (~40–60 µm).

- The tiny aluminum particles are pervasive and coat everything.

From this work, a much better understanding of the small-caliber ammunition ignition event has been gained. The authors of this work continue to work closely with the primer modelers in an effort to provide physical understanding of the no. 41 primer. Ongoing efforts will be aimed at further characterizing the basic primer output to include heat flux and temperature measurements.

7. References

1. Brosseau, T. M. *Development of the Minihat Pressure Transducer for Use in the Extreme Environments of Small Caliber Gun Barrels*; BRL-MR-2072; U.S. Army Ballistic Research Laboratory: Aberdeen Proving Ground, MD, 1970.

2. Chang, L. M.; Rocchio, J. J. *Simulator Diagnostics of the Early Phase Ignition Phenomena in a 105-mm Tank Gun Chamber*; BRL-TR-2890; U.S. Army Ballistic Research Laboratory: Aberdeen Proving Ground, MD, 1988.

3. Ruth, C. R.; Minor, T. C. *Experimental Study of Flamespreading Processes in 155-mm, XM216 Modular Propelling Charges*; BRL-MR-3840; U.S. Army Ballistic Research Laboratory: Aberdeen Proving Ground, MD, June 1990.

4. Chang, L. M. *Interior Ballistic Simulations of 25-mm Gun Charges*; BRL-TR-3330; U.S. Army Ballistic Research Laboratory: Aberdeen Proving Ground, MD, 1992.

5. Zoltani, C. K. *M-82 Primer Flow Study*; BRL-TR-02084; U.S. Army Ballistic Research Laboratory: Aberdeen Proving Ground, MD, 1978.

6. May, I. W.; Horst, A. W. *Charge Design Considerations and Their Effect on Pressure Waves in Guns*; BRL-TR-02277; U.S. Army Ballistic Research Laboratory: Aberdeen Proving Ground, MD, 1980.

7. Nusca, M. U.S. Army Research Laboratory. Private communication, 2005.

8. Kuo, K.; Moore, B.; Chen, D. *Characterization of Mass Flow Rates for Various Percussion Primers*; Gasdynamics of Detonations and Explosives; J. R. Bowen, N. Manson, A. K. Oppenheim, R. I. Soloukhin, Eds.; AIAA Progress Series, Vol. 75, 1981, pp 323–337.

9. Ekstedt, E. E.; Vest, D. C.; Emerson, V. C.; Dean, L. W. *Pressure Studies of Artillery Primers Fired Statically*; BRL-TR-938; U.S. Army Ballistic Research Laboratory: Aberdeen Proving Ground, MD, 1955.

10. Engineering Laboratories, Inc. www.plasticballs.com (accessed xxxx), 0.8-mm-diameter Teflon spheres source.

11. Conroy, P. U.S. Army Research Laboratory. Private communication, 2005.

12. Vest, D. C.; Anders, J. E.; Grollman, B. B.; DeMare, B. L. *Ballistic Studies with a Microwave Interferometer*, *Part 1*; BRL-TR-968; U.S. Army Ballistic Research Laboratory: Aberdeen Proving Ground, MD, 1955.

13. Vest, D. C.; Anders, J. E.; Smith, H. C.; DeMare, B. L.; Grollman, B. B.; Kashihara, T. *Ballistic Studies with a Microwave Interferometer*, *Part 2*; BRL-TR-1006; U.S. Army Ballistic Research Laboratory: Aberdeen Proving Ground, MD, 1955.

14. Nusca, M. J. CFD Model of the Plasma Efflux Generated by an ETC Igniter: Characterization of Propellant Surface Conditions. *Proceedings of the 38th JANNAF Combustion Subcommittee Meeting*; CPIA Publication 712, April 2002, pp 279–297.

15. Zoltani, C. K.; Bicen, A. F.; Coleman, M. W. *Flow Visualization in a Particle Laden Jet Flow*; BRL-TR-3134; U.S. Army Ballistic Research Laboratory: Aberdeen Proving Ground, MD, 1990.

16. http://ww.chemguide.co.uk/inorganic/group2/thermstab.html#top: the Chemguides's inorganic menu to understanding Chemistry (accessed 24 October 2005).

17. Conroy, P. U.S. Army Research Laboratory. Private communication, February 2006.

18. Weinacht, P.; Newill, J. F.; Conroy, P. J. *Conceptual Design Approach for Small Caliber Aeroballistics with Application to 5.56-mm Ammunition*; ARL-TR-3620; U.S. Army Research Laboratory: Aberdeen Proving Ground, MD, 2005.

NO. OF
COPIES   ORGANIZATION

1   DEFENSE TECHNICAL
(PDF   INFORMATION CTR
ONLY)   DTIC OCA
        8725 JOHN J KINGMAN RD
        STE 0944
        FORT BELVOIR VA 22060-6218

1   US ARMY RSRCH DEV &
        ENGRG CMD
        SYSTEMS OF SYSTEMS
        INTEGRATION
        AMSRD SS T
        6000 6TH ST STE 100
        FORT BELVOIR VA 22060-5608

1   DIRECTOR
        US ARMY RESEARCH LAB
        IMNE ALC IMS
        2800 POWDER MILL RD
        ADELPHI MD 20783-1197

3   DIRECTOR
        US ARMY RESEARCH LAB
        AMSRD ARL CI OK TL
        2800 POWDER MILL RD
        ADELPHI MD 20783-1197

        ABERDEEN PROVING GROUND

1   DIR USARL
        AMSRD ARL CI OK TP (BLDG 4600)

)

1	PRODUCT MGR SMALL AND MEDIUM CALIBER AMMO SFAE AMO MAS SMC M BUTLER BLDG 354 PICATINNY ARSENAL NJ 07806-5000
1	PROJECT MGR MANEUVER AMMUNITION SYSTEMS SFAE AMO MAS SMC R KOWALSKI BLDG 354 PICATINNY ARSENAL NJ 07806-5000
1	ATK R DOHRN MN07-LW54 4700 NATHAN LN N PLYMOUTH MN 55442
1	ATK C AAKHUS MN07-LW54 4700 NATHAN LN N PLYMOUTH MN 55442
1	ATK M JANTSCHER MN07-LW54 4700 NATHAN LN N PLYMOUTH MN 55442
1	ATK LAKE CITY K ENLOW PO BOX 1000 INDEPENDENCE MO 64051-1000
5	ATK LAKE CITY SMALL CALIBER AMMO LAKE CITY ARMY AMMO PLANT D MANSFIELD PO BOX 1000 INDEPENDENCE MO 64051-1000
1	ATK LAKE CITY SMALL CALIBER MO10-003 LAKE CITY ARMY AMMO PLANT J WESTBROOK PO BOX 1000 INDEPENDENCE MO 64051-1000

1	ALLIANT TECHSYSTEMS INC D KAMDAR MN07-LW54 4700 NATHAN LN N PLYMOUTH MN 55442-2512
1	ATK ORDNANCE SYS B BECKER MN07-MW44 4700 NATHAN LN N PLYMOUTH MN 55442-2512
1	US ARMY TACOM ARDEC CCAC AMSTA AR CCL C G FLEMING BLDG 65N PICATINNY ARSENAL NJ 07806-5000
1	US ARMY TACOM ARDEC CCAC AMSTA AR CCL B J MIDDLETON BLDG 65N PICATINNY ARSENAL NJ 07806-5000
1	US ARMY TACOM ARDEC ASIC PROGRAM INTEGRATION OFC J RESCH BLDG 1 PICATINNY ARSENAL NJ 07806-5000
1	US ARMY TACOM ARDEC M MINISI BLDG 65N PICATINNY ARSENAL NJ 07806-5000
1	US ARMY TACOM ARDEC S SPICKERT-FULTON BLDG 65 PICATINNY ARSENAL NJ 07806-5000
1	US ARMY TACOM ARDEC AMSRD AAR AEM T M NICOLICH BLDG 65S PICATINNY ARSENAL NJ 07806-5000

1 US ARMY TACOM ARDEC
   AMSRD AAR AEM
   S MUSALLI
   BLDG 65S
   PICATINNY ARSENAL NJ
   07806-5000

1 US ARMY TACOM ARDEC
   AMSRD AAR AEM I
   R MAZESKI
   BLDG 65N
   PICATINNY ARSENAL NJ
   07806-5000

1 US ARMY TACOM ARDEC
   A FARINA
   BLDG 95
   PICATINNY ARSENAL NJ
   07806-5000

1 US ARMY TACOM ARDEC
   CCAC
   AMSRD AAR AEM I
   D CONWAY
   BLDG 65N
   PICATINNY ARSENAL NJ
   07806-5000

1 US ARMY TACOM ARDEC
   AMSTA AR FSF T
   H HUDGINS
   BLDG 382
   PICATINNY ARSENAL NJ
   07806-5000

1 US ARMY TACOM ARDEC
   CCAC AMSTA AR CCL D
   F HANZL
   BLDG 382
   PICATINNY ARSENAL NJ
   07806-5000

1 US ARMY TACOM ARDEC
   P RIGGS
   BLDG 65N
   PICATINNY ARSENAL NJ
   07806-5000

1 OPM MAS
   SFAE AMO MAS MC
   G DEROSA
   BLDG 354
   PICATINNY ARSENAL NJ
   07806-5000

1 SIERRA BULLETS
   P DALY
   1400 WEST HENRY ST
   SEDALIA MO 65302-0818

1 ST MARKS POWDER
   GENERAL DYNAMICS
   R PULVER
   7121 COASTAL HWY
   CRAWFORDVILLE FL 32327

1 ST MARKS POWDER
   GENERAL DYNAMICS
   J DRUMMOND
   7121 COASTAL HWY
   CRAWFORDVILLE FL 32327

1 ST MARKS POWDER
   GENERAL DYNAMICS
   J HOWARD
   7121 COASTAL HWY
   CRAWFORDVILLE FL 32327

1 RADFORD ARMY AMMO PLNT
   K BROWN
   PO BOX 1 RT 114
   RADFORD VA 24143

1 RADFORD ARMY AMMO PLNT
   W WERRELL
   PO BOX 1 RT 114
   RADFORD VA 24143

1 RADFORD ARMY AMMO PLNT
   H ZIEGLER
   PO BOX 1 RT 114
   RADFORD VA 24143

ABERDEEN PROVING GROUND

1 COMMANDER
   US ARMY ARDEC
   FIRING TABLES & BALLISTICS DIV
   AMSRD AAR AEF T
   B TILGHMAN
   2201 ABERDEEN BLVD
   APG MD 21005-5001

   1   COMMANDER
         US ARMY ARDEC
         FIRING TABLES & BALLISTICS DIV
         AMSRD AAR AEF T
         F MIRABELLE
         2201 ABERDEEN BLVD
         APG MD 21005-5001

  28   DIR USARL
         AMSRD ARL WM B
           J NEWILL
           M ZOLTOSKI
         AMSRD ARL WM BA
           D LYON
           S WANSACK
         AMSRD ARL WM BC
           M BUNDY
           J DESPIRITO
           J GARNER
           B GUIDOS
           K HEAVEY
           P PLOSTINS
           J SAHU
           S SILTON
           D WEBB
         AMSRD ARL WM BD
           A BRANT
           J COLBURN
           P KASTE
           A WILLIAMS (3 CPS)
         AMSRD ARL WM BF
           W OBERLE
           R PEARSON
           S WILKERSON
         AMSRD ARL WM M
           J MCCAULEY
           S MCKNIGHT
          AMSRD ARL WM MB
           J SOUTH
          AMSRD ARL WM TA
           M BURKINS
          AMSRD ARL WM TC
           L MAGNESS
           B PETERSON

INTENTIONALLY LEFT BLANK.